

ON THE DISSOLUTION CHARACTERISTICS OF
Kr-BOMBARDED LITHIUM FLUORIDE

ON THE DISSOLUTION CHARACTERISTICS OF
KRYPTON-BOMBARDED LITHIUM FLUORIDE

BINOY KUMAR SINHA, B.Sc. (HONS.), M.Sc. (PHYS.)

A Thesis

Submitted to the School of Graduate Studies
in Partial Fulfilment of the Requirements

for the Degree

Master of Science

McMaster University

July, 1972

MASTER OF SCIENCE (1972)

McMASTER UNIVERSITY
Hamilton, Ontario

TITLE: On the Dissolution Characteristics of Kr-bombarded Lithium
Fluoride

AUTHOR: B. K. Sinha, B.Sc. (Hons.-Physics) (Patna University, India)
M.Sc. (Phys.) (Patna University, India)

SUPERVISOR: Professor M. B. Ives

NUMBER OF PAGES: x, 67

SCOPE AND CONTENTS:

A study has been made of crystal dissolution of Kr-bombarded lithium fluoride in aqueous solutions of ferric chloride. Bombarded surfaces were observed to have a higher dissolution rate than the non-bombarded ones, the dissolution rate itself being a function of ion-concentration. A bombarded and annealed surface was found to have an even higher dissolution rate than a bombarded surface.

Nucleation of pits was observed to depend on the dose of bombardment. A dose of 10^{15} and 10^{16} ions/cm² caused uniform dissolution of the surface without any pit-formation but a dose of 10^{13} and 10^{14} ions/cm² was found to cause pitting even in the presence of radiation damage as indicated by the activity of the radioactive krypton. In the former case uniform dissolution is explained by the relative increase in the density of Frenkel defects.

ACKNOWLEDGEMENTS

The author wishes to thank Professor M. B. Ives for his constant supervision throughout the course of this work and Professor Roger Kelly for his valuable discussions and guidance.

Thanks are extended to Messrs. Ted Parker and D. K. Murti for their active cooperation in the experimental work.

The author greatly appreciates the study-leave granted to him by the authorities of Bhabha Atomic Research Center, India.

The author wishes to acknowledge the receipt of a McMaster Graduate Scholarship and the aid of a research grant from the National Research Council of Canada.

The author expresses his thanks to Veronica Komczynski for typing the manuscript.

TABLE OF CONTENTS

	Page
INTRODUCTION	
CHAPTER 1: THE DISSOLUTION THEORY	
1.1 The Basic Approach	1
1.2 The Mechanistic Approach	2
1.3 Analytical Approach to Two Dimensional Nucleation	3
1.4 Nucleation at Point Defects	4
1.5 Nucleation at Extended Defects	5
1.6 Impurities and Inhibited Dissolution	6
CHAPTER 2: DEFECTS IN LITHIUM FLUORIDE	8
2.1 The Defects	8
2.2 The Structure	8
2.3 Schottky and Frenkel Defects	8
2.4 Vacancy Pairs and Complexes	11
2.5 The Dislocations	11
2.6 Radiation Induced Defects	13
2.7 The Structural Changes	13
2.8 New Dislocation Sources	14
2.9 Effects on Etching	14
CHAPTER 3: EXPERIMENTAL TECHNIQUES	15
3.1 A Simple Description	15
3.2 Bombardment and Counting Techniques	17
3.3 The Error Estimation	19
3.3.1 The Etch-Time	19
3.3.2 The Interference Fringe Shift	19
3.3.3 The Irradiation Dose	20
3.3.4 Error from Counting and Calculations	20

	Page
CHAPTER 4: EXPERIMENTAL RESULTS	22
4.1 A Summary	22
4.2 The Dissolution Experiments	23
4.3 Effect of Annealing	24
4.4 Stripping Experiments	25
4.5 Optical Metallographic Observations	27
4.6 Replica Electron Microscopy	29
CHAPTER 5: A DISCUSSION	30
5.1 On the Dissolution Experiments	30
5.2 On the Stripping Experiments	32
5.2.1 A Macroscopic Approach	32
5.2.2 The Microscopic Approach	34
5.2.3 Fe ⁺⁺⁺ Ion Concentration and Nucleation of Pits	36

LIST OF FIGURES

1. Kossel model of a crystal surface showing close packed {100} surface, ledges and kinks.
2. Two dimensional model of a general surface represented by an array of ledges.
3. Two types of kinks in a surface ledge which may be hosts to inhibitor ions (filled circles).
4. The lithium fluoride crystal structure. The space lattice is fcc, and the basis has one Li^+ ion at 0, 0, 0 and one F^- ion at 1/2, 1/2, 1/2.
5. Two dimensional perfect crystal.
6. Frenkel defects (interstitial cations and anions with corresponding vacancies).
7. Schottky defect (cation and anion vacancies).
8. Vacancy pair and divalent ion-vacancy complex in lithium fluoride.
9. Comparison of stress for (100) glide with stress for (110) glide in LiF crystals.
10. A typical surface arrangement after etching. A)Side view, B)Top view.
11. Target arrangement for ion-bombardment.
12. An arrangement for the ion source.
13. Crystal Dissolution vs. Etch-Time, 10 ppm Fe^{+++} (etch-interval \approx 7.5 sec).
14. Crystal Dissolution vs. Etch-Time (etch-interval 30 sec), 10 ppm Fe^{+++} .
15. Crystal Dissolution vs. Etch-Time, 2 ppm Fe^{+++} .
16. Crystal Dissolution vs. Etch-Time, 0 ppm Fe^{+++} .
17. Dissolution rate vs. Fe^{+++} ion concentration.
18. Normalised Activity vs. etch time on Unannealed and bombarded and annealed and bombarded surfaces.

19. Normalised Activity vs. Etch Time (Dose 10^{16} ions/cm², energies 35 keV, 15 keV, 5 keV).
20. Absolute Activity vs. Etch Time (Energy 15 keV, Doses 10^{16} , 10^{15} , 10^{14} , 10^{13} ions/cm²).
21. Absolute Activity vs. Etch Time (at 1000, 500, 100, 10 ppm ion concentration).
22. Figure represents A - an unetched surface; B - a surface bombarded at a dose of 10^{16} ions/cm² and etched for 30 sec in a 10 ppm Fe⁺⁺⁺ solution, C - an unbombarded surface etched in the same way as B. Mag. 256X.
23. Figures A and C bombarded at a dose of 10^{16} ions/cm² and etched for 30 seconds and 60 seconds respectively in 10 ppm Fe⁺⁺⁺ solution. B and D are unbombarded surfaces etched for 30 and 60 seconds respectively. Mag. 256X.
24. Figure represents A and B bombarded at a dose of 10^{15} ions/cm² and etched for 5 sec and 25 sec in a 10 ppm Fe⁺⁺⁺ solution. Mag. 256X.
25. A and B are unbombarded surfaces etched for 5 sec and 25 sec respectively (opposite face of the same sample as in fig. 24). Mag. 256X.
26. A is unetched surface. B is bombarded by a dose of 10^{14} ions/cm² and etched for 3 seconds in a 10 ppm Fe⁺⁺⁺ solution. Mag. 256X.
27. Interference micrograph of the sample represented by fig. 22.
28. Interference micrograph of the sample represented by fig. 23.
29. Interference micrograph of the sample represented by fig. 24.
30. Interference micrograph of the sample represented by fig. 25.
31. Replica electron micrograph of the region B of fig. 22 and A of fig. 23.
 A → Mag., 2,500X
 B → Mag., 500X

C → 10,000X

D → 22,500X

32. Replica-electron micrograph of a sample bombarded at a dose of 10^{15} ions/cm² and etched in a 10 ppm Fe⁺⁺⁺ solution.
- A → A junction of the bombarded surface after 5 sec and 25 sec etch.
Mag. 2,500X.
- B → Same junction at 7,500X.
- C and D → Bombarded surface after 5 sec etch. Mag. 10,000X and 22,500X respectively.
33. A, B, C, D and E represent an electron micrograph of etching sequence after 0, 5, 10, 15 and 20 sec etch at a magnification of 5000X. The sample was bombarded at a dose of 10^{15} ions/cm² and in a 10 ppm etchant.
34. A sketch showing a preferential attack at a dislocation site.
35. A sketch to estimate critical distance between two dissolution nuclei for a non-preferential attack at a dislocation site.

INTRODUCTION

The period of the last ten years has given us a reasonable amount of literature on the dissolution morphology of lithium fluoride surfaces as well as on the role of inhibitor-ions on the mechanism of their dissolution. In the present work we have made some attempts to study the dissolution characteristics of krypton-bombarded lithium fluoride in aqueous solutions of ferric chloride.

The first series of experiments was conducted to measure the dissolution rates on Kr-bombarded lithium fluoride as well as non-bombarded specimens with a view to examining the roles of ferric ions on the crystal dissolution. The effect of annealing of the irradiated samples on the crystal dissolution rate was also examined.

The second series of experiments were conducted to examine the role of radiation damage on the development of the pits on the etched surfaces. The dose of irradiation as well as the energy of irradiation were used as variables for the experiment. Radioactive krypton was used to estimate the depth of damage.

The dose of irradiation was observed to have a dominating role on the development of the pits. For a dose of 10^{13} and 10^{14} ions/cm², the pitting on the bombarded surface took place nearly simultaneously as on the unbombarded surface except that the size of the pits on the bombarded surface was found to be smaller than that on the unbombarded surface. On irradiation by a dose of 10^{15} or 10^{16} ions/cm², pitting was only found to take place when the considerable radiation damage was etched out. This

conclusion was supported by an examination on 1) the optical microscope, 2) interference microscope as well as on 3) electron microscope by plastic replication technique.

No evidence for radiation-induced pits was observed. At the same time the dislocation density on samples of radiated and irradiated "cleavage-pair" specimens was always found to be the same, within experimental errors.

As a result of the above mentioned investigations it is concluded that the ratio of the dissolution rates on the bombarded and non-bombarded surface is a function of Fe^{+++} ion concentration in the solvent. It is found to vary from 1 to about 2 for an ion concentration range of 0 ppm to 10 ppm.

From a theoretical analysis it is concluded that uniform dissolution rate at the higher radiation doses are due to dissolution-nucleation at defect-clusters and not at isolated point defects. It is further concluded that for a radiation dose of 10^{15} ions/cm² or more the average distance between defect-clusters is less than 80\AA and for a dose of 10^{14} ions/cm² or less this distance is more than 80\AA .

CHAPTER 1
THE DISSOLUTION THEORY

1.1 The Basic Approach

The theoretical analysis of crystal dissolution can be classified into two categories: 1) the one which is based on the mechanistic theory of Burton, Cabrera and Frank (1), and 2) the one which applied the topological theory of Frank (2), Cabrera and Vermilyea (3) and that of Chernov (4). While the first treatment is based on the Kossel (5) and Stranski (6) model of a surface composed of close-packed planes separated by monoatomic ledges containing kinks, the second one can be treated as general.

Frenkel (7), and Burton and Cabrera (8) have shown that the steps on a crystal surface contain a high concentration of kinks. When a crystal dissolves, material is lost preferentially from the kinks, where binding is the weakest, thereby affecting the motion of the kinks along the ledges. By travelling the length of a ledge, a kink can produce an overall motion of that ledge by an amount equal to the offset of the kink. The localised dissolution rate will be proportional to the product of the ledge velocity (v) and the concentration of the ledges (k) in the adjoining area. Fig. 1 represents a Kossel model of a crystal surface showing $\{100\}$ surfaces, ledges and kinks. Fig. 2 shows a two dimensional model of a general surface represented by an array of ledges. The problem is then reduced to theoretically interpreting how the ledge velocity depends on the ledge density.

In the mechanistic approach Burton et al. (1) used the ledge model and derived an expression for the ledge velocity as a function of the ledge density but in the case of the topographical approach Frank assumed a form for $V(k)$ i.e. the ledge velocity, and developed a theory.

1.2 The Mechanistic Approach

It is already established by Frenkel (7) and Burton et al. (1) that at room temperature every crystal surface has a high concentration of kinks along existing steps due to thermal fluctuations. The latter investigators have further indicated a comparative difficulty for the formation of surface steps on an otherwise perfect crystal surface in equilibrium with its vapour or solution well below the melting point of the material under consideration. Availability of surface-steps is essential for the very process of crystal dissolution. Therefore, the more perfect a crystal surface, the less the dissolution to be expected.

When a receding step reaches the edge of a crystal surface, it is eliminated. Therefore, for the dissolution process to continue, the surface must provide a source of steps. In the case of a screw dislocation there is no problem because the step is never eliminated. Hirth and Pound (9) have examined the role of crystal edges as a source of surface steps during evaporation and have studied the problem in detail. Apart from the crystal edges they have further studied the role of surface imperfections like pores, cracks and dislocations on the evaporation coefficient of the crystal.

Therefore when we consider a perfect region of a crystal surface far from surface-imperfections or any other sources of surface steps, the formation of surface steps is made possible only by two dimensional

nucleation which can occur only at high undersaturations. Hence, for the formation of dislocation etch-pit, the intersection of the dislocation with the surface must provide a higher rate of two dimensional nucleation than the surrounding surface.

1.3 Analytical Approach to Two Dimensional Nucleation

Let us consider a perfect surface and find an analytical expression for the two-dimensional nucleation for dissolution. Let

ΔG = free energy for the formation of a two dimensional nucleus

r and h = radius and depth of the nucleus

γ = surface energy

Ω = the atomic volume

$\Delta\mu_0$ = the change in chemical potential when a molecule of the crystal goes into solution. $\Delta\mu_0$ can also be written as

$$\Delta\mu_0 = kT \ln c/c_0 \quad (1.1)$$

where k = Boltzmann constant

T = Temperature

c_0 = Equilibrium concentration of crystal in the solvent

c = The actual concentration

The free energy G consists of a volume and a surface energy term and can be written as

$$G = \frac{\pi r^2 h}{\Omega} \Delta\mu_0 + 2\pi r h \cdot \gamma \quad (1.2)$$

The radius of the critical nucleus, ρ_c , is defined by the condition that ΔG is a minimum with respect to r , and nuclei smaller than ρ_c will shrink while larger ones will grow. Therefore, the condition for the formation of critical nucleus is

$$\frac{\partial G}{\partial r} = 0 \quad (1.3)$$

$$\text{or } \frac{2\pi r \cdot h}{\Omega} \Delta\mu_0 + 2\pi h \cdot y \Big|_{r=\rho_c} = 0$$

Solving for ρ_c we get the expression

$$\rho_c = \frac{\Omega y}{\Delta\mu_0} = -\frac{\Omega y}{kT \ln c/c_0} \quad (1.4)$$

Therefore the activation energy ΔG for the formation of a two-dimensional nucleus can be obtained by putting ρ_c for r in (1.2), or

$$\Delta G = -\frac{\pi y^2 \Omega h}{kT \ln c/c_0} \quad (1.5)$$

1.4 Nucleation at Point Defects

Point defects in lithium fluoride crystals chiefly consist of (1) Schottky defects, (2) Frenkel pairs and (3) colour centers. Schottky defects or vacancies may further give rise to a divacancy or a vacancy-cluster consisting of a number of vacancies. Among the extended defects vacancy discs, loops and spheres may be mentioned apart from the dislocations. Let E_f represent the formation energy of such defects or the excitation energy in the case of colour centers. The effect of this energy E_f is to reduce the energy for formation of a two dimensional nucleus and this will be less than that of a perfect surface and can be written as

$$G = \frac{\pi r^2 h}{\Omega} \Delta\mu_0 + 2\pi r h y - E_f \quad (1.6)$$

By putting the expression for E_f for each case in (6) the condition for the formation of a critical nucleus can be obtained as in the case of a perfect surface and similarly the activation energy.

1.5 Nucleation at Extended Defects

The case of vacancy-discs, loops and spheres may be treated as in the previous section for each individual case. Since dislocations are the most important of all the extended defects, they can be dealt with separately and in detail.

Since a dislocation has a strain energy associated with it, the free energy for formation of a two-dimensional nucleus will be similarly less than that for a perfect surface

$$G = \frac{\pi r^2 h}{\Omega} \Delta\mu_0 + 2\pi r h \gamma - hE(r) \quad (1.7)$$

where $E(r)$ is the strain energy within a cylinder of radius r , per unit length of the dislocation line. The total strain energy can be summed up as equal to the elastic strain energy and the core energy E_c . The elastic strain energy for a dislocation is given by (10)

$$E(r) = \frac{G' b^2}{4\pi(1-\nu)} \ln r/r_0 \quad (\text{for edge}) \quad (1.8)$$

$$E(r) = \frac{G' b^2}{4\pi} \ln r/r_0 \quad (\text{for screw}) \quad (1.9)$$

where G' = Elastic shear modulus of the crystal

b = Burger's vector

r_0 = radius of the core

ν = the Poisson ratio

r = outer limit of integration in calculating the energy.

If there is a single dislocation in a crystal, r is the radius of the crystal; otherwise it is taken to be equal to average spacing between dislocations. The strain energy of the dislocation can therefore be written as

$$E(r) \approx E_c + \frac{G' b^2}{4\pi} \ln r/r_0 \quad (1.10)$$

Since $E(r) > 0$, the activation energy for two dimensional nucleation at a dislocation site will be lower than that on a perfect surface. Cabrera, Levine and Plaskett (11,12,13) have treated this problem by ignoring the core energy E_C .

$$G = \frac{\pi r^2 h}{\Omega} \Delta\mu_0 + 2\pi r h y - \frac{G' b^2 h}{4\pi} \ln r/r_0 \quad (1.11)$$

To find the condition for the formation of a two dimensional nucleus

$$\frac{\partial G}{\partial r} = 0, \text{ hence}$$

$$\frac{2\pi h \cdot \Delta\mu_0}{\Omega} r^2 + 2\pi r h \cdot y - \frac{G b^2 h}{4\pi} = 0 \quad (1.12)$$

This quadratic equation in r has two solutions

$$r_1 = \frac{\rho_C}{2} \left[1 - \left(1 - \frac{4r_C}{\rho_C} \right)^{1/2} \right] \quad (1.13)$$

$$\text{and } r_2 = \frac{\rho_C}{2} \left[1 + \left(1 - \frac{4r_C}{\rho_C} \right)^{1/2} \right] \quad (1.14)$$

where $r_C = \frac{G' b^2}{8\pi^2 y}$

There is a maximum at r_2 and a minimum at r_1 . Cabrera and Levine (11) have pointed out that as $\Delta\mu_0$ is increased by decreasing c/c_0 , r_1 and r_2 approach each other and finally when $\rho_C = 4r_C$, r_1 becomes equal to r_2 . They interpret this as meaning that at sufficiently great undersaturations (low c/c_0), the dislocation core opens up and there is no need to nucleate new layers.

1.6 Impurities and Inhibited Dissolution

When a solvent contains a small amount of foreign matter which adsorbs strongly to the surface, it can give rise to a protective effect,

reducing the velocity with which the step on the crystal surface travels. The impurity is removed and rendered ineffective when the step goes by. In the case of dissolution of lithium fluoride, Gilman, Johnston and Sears (14) originally suggested that the most suitable site for the incorporation of Fe^{+3} ions into the surface would be at kink positions where they could be surrounded by neighbouring F^- ions of the crystal (as at B in Figure 3). Ives and Baskin (15) have preferred, however, to consider the A kink-pairs as the principal sites for adsorption. The role of the inhibitor ions is to hold up the kinks which will otherwise quickly traverse their ledges until annihilated by kinks of opposite sense.

CHAPTER 2

DEFECTS IN LITHIUM FLUORIDE

2.1 The Defects

Defects in lithium fluoride as in the case of any other solids and specially as in the case of alkali halides can be grouped into two major categories:

- 1) Point defects which may consist of Schottky defects or vacancies, Frenkel defects and colour centers.
- 2) Extended defects which may consist of vacancy-clusters, vacancy-discs, loops or spherical voids under suitable circumstances (16). But the most important of all the extended defects are dislocations.

2.2 The Structure

Lithium fluoride is a typical ionic compound. It crystallises in the rock salt structure, Fig. 4. In this structure each cation (alkali metal ion) is surrounded by six nearest neighbour anions (halogen ions), and each anion by six nearest neighbour cations. The cations and anions are each situated on the points of separate face-centered cubic lattices, and these two lattices are interleaved with each other.

2.3 Schottky and Frenkel Defects

It is well known that all alkali halides including lithium fluoride show electrical conductivity at elevated temperatures. This is true of all the polar crystals. Frenkel (17) explained it by pointing out that this type of conductivity required the postulation of mobile charged imperfections in real crystals. Interstitial ions and vacant lattice sites are

imperfections which have the properties necessary to explain the transport of matter that is observed in electrolysis or diffusion experiments. Fig. 5 shows a two dimensional representation of lithium fluoride crystal free from any defects.

In figure 6 a crystal is shown with two types of interstitial ions. One of these, Li^+ , arises when a cation is removed from its normal site by some process and placed in an interstitial position; the other, F^- , i.e. the fluorine ion vacancy, arises when an anion is similarly displaced. As one moves either the cation or the anion to an interstitial position, one creates a corresponding vacant lattice site - either a cation vacancy or an anion vacancy. These imperfections are also shown in figure 6. This mechanism of defect formation is called the Frenkel mechanism, and the dual imperfection - the interstitial ion together with the vacancy - is known as a Frenkel defect.

Vacant lattice sites in a crystal may be formed in another way, which does not involve the production of interstitial ions. This is illustrated in figure 7, where cations and anions are both removed from the interior of the crystal and added to the surface to form a new layer of the crystal. In order for this process to occur appreciably, equal number of cations and anions must be placed on the surface to preserve electrical neutrality, and hence equal concentrations of cation and anion vacancies are produced in the interior of the crystal. This mechanism of vacancy production was suggested by Wagner and Schottky (18,19). The dual imperfection consisting of a cation vacancy and an anion vacancy is known as a Schottky defect.

Frenkel and Schottky defects arise in real crystals for thermodynamic reasons. For a crystal to be in thermodynamic equilibrium at a given temperature, its free energy must be minimum. Although energy must be expended to form a defect against the cohesive forces of the crystal, the increase in entropy resulting from the defect causes the free energy to be a minimum for a definite concentration of defects at a given temperature. If W_i and W_s are the energies required to form a Frenkel and Schottky defects respectively and n_i and n_v are numbers of ions in interstitial positions and vacant lattice sites at equilibrium per unit volume, then it can be derived that

$$n_i = \sqrt{ANN_i} \exp(-W_i/2kT) \quad (1)$$

$$n_v = BN \exp(-W_s/2kT) \quad (2)$$

where A and B are constants

N = Total no. of lattice points/vol.

N_i = Total no. of possible interstitial positions/vol.

k = Boltzmann constant

T = Temperature

In any crystal then, Schottky defects as well as cationic and anionic Frenkel defects are to be expected from purely thermodynamic causes. However, because of larger radii of anions, the energy required to place them into interstitial positions is considerably greater than that required to place cations interstitially. Generally, therefore, cationic Frenkel defects are to be expected to form more easily than anionic ions. Calculations of the energy of formation of Schottky and Frenkel defects indicate that the former type is favoured if there is approximate equality in size

of the cations and anions, if the dielectric constant is low, and if the Van der Waals contribution to the lattice energy is low. Frenkel defects are favoured when there is a considerable difference in ionic sizes and when the dielectric constant and Van der Waals energy are high.

2.4 Vacancy Pairs and Complexes

Vacancies and interstitial ions are local regions of unbalanced charge in the crystal. Thus a cation vacancy bears an effective negative charge and an anion vacancy effective positive charge. This causes an electrostatic attraction between the two defects leading to the formation of a double vacancy or "pair", with the cation and anion vacancies residing on two adjacent sites, fig. 8. The binding energy of such a pair can be readily estimated from the lattice constant and the dielectric constant of the crystal. This energy is reasonably of the order of $W_5/2$ and a substantial concentration of such pairs is, therefore, to be expected (20).

Although the vacancy pairs are electrically neutral entities and do not contribute to the electrical conductivity, they can move through the crystal and thus contribute to diffusion processes. Their possible existence is, therefore, important to colour center problems.

2.5 The Dislocations

Dislocations are the most important of the extended defects. The dislocation contents of the as grown lithium fluoride range from about 3×10^4 dislocations/cm² in better crystals to about 10^5 /cm² in poorer ones. About half the dislocations are found to be in sub-grain boundaries, and half in the interior of the sub-grains. The dislocation structures of the as grown crystals do not depend on the impurity content consistent with

the findings of Washburn and Nadeau (21). They concluded that the dislocation content was insensitive to growth rate, impurities and temperature gradient in the solid. Most of the dislocations in melt grown crystals result from accidental thermal and mechanical stresses.

Lithium fluoride crystals prefer to glide plastically on $\{110\}$ planes and in $\langle\bar{1}10\rangle$ directions, as do most alkali halides that have the rock-salt structure. The $\langle 110\rangle$ directions in the rock-salt structure are the only low index directions that lie parallel to rows of ions of the same charge sign, and glide can occur in these directions without juxtaposing ions of the same sign. Also, the smallest crystallographic repeat distance, i.e. the distance between neighbouring atoms that repeat, lies in the $\langle 110\rangle$ direction. Since the energy of the dislocation line is proportional to the square of the slip vector the energy of a dislocation with a $\langle 110\rangle$ vector is lower than that of other dislocations (22).

For a given glide direction, metal crystals normally prefer to glide on whatever crystal planes have the widest spacing. This is not the case for lithium fluoride which prefers to glide on $\{110\}$ planes even though its $\{100\}$ planes are more widely spaced. At temperatures above 300°C glide does occur readily on $\{100\}$ planes (23), but the preference for $\{110\}$ planes is strong at lower temperatures, figure 9. It is thought that the $\{110\}$ planes are preferred over $\{100\}$ planes because the core energy of a dislocation is considerably smaller for the $\{110\}$ planes (24) and particularly because the variation of the core energy with position of a dislocation on its glide plane is smaller.

2.6 Radiation Induced Defects

Extensive work has been done on the high energy bombardment of lithium fluoride crystals by neutrons (25) but so far no quantitative studies have been made on the low energy high mass bombardment of lithium fluoride. The high mass of the bombarding particle has a major role in transfer of incident energy to the lattice atoms. Lithium fluoride is also damaged by irradiation with X-rays or γ -rays. The extent of damage, as indicated by the property changes, is about the same as for neutron irradiation when the colours of the damaged crystals are the same. Thus the dominant part of the damage is caused by ionisation.

2.7 The Structural Changes

Colouration is the most striking effect of radiation. As little radiation as 10^{10} nvt causes a detectable F-band absorption in the ultra-violet at 2500 A° wavelength. The tail of the F-band causes very pale yellow coloration to appear at 10^{12} nvt which becomes canary yellow at 10^{13} nvt, deep yellow at 10^{14} nvt, reddish brown at 10^{15} nvt, and completely black at 10^{16} nvt. Substantial hardening occurs as the dose increases from 10^{12} to 10^{16} nvt. Lattice expansion becomes detectable at 10^{16} nvt and increases to about 0.4% after an irradiation of 5×10^{17} nvt. Finally cavities and thin platelets of Li metal along {100} planes appear when the dose reaches about 10^{18} nvt (26).

No evidence of the direct production of dislocations at displacement spikes has been found in as irradiated crystals (25). Thus no local collections of small dislocation loops appeared and no isolated loops larger than about 25A in size are formed. This is unlike the case of damage by

fission fragments which produces heavy and easily detectable tracks (27). Extended irradiation produces clustering of the isolated defects that appear for small doses.

2.8 New Dislocation Sources

Radiation damage sometimes can put dislocation sources into a crystal by inducing the formation of precipitate particles (25). It has been found that this only occurs in impure crystals.

2.9 EFFECTS ON ETCHING: Gilman and Johnston have observed a rather uniform roughening of the surface on etching for exposures greater than about 10^{15} nvt which did not change much with further exposure. They concluded that this rough etching is not caused by individual point defects and expressed the doubt whether etch pits caused by individual point defects could be seen.

The electron bombarded crystals gave an etching effect much like the effect observed after neutron bombardment. They concluded that aggregated Frenkel defects were responsible for the etching effect.

CHAPTER 3

EXPERIMENTAL TECHNIQUES

3.1 A Simple Description

Experiments were performed on cleaved {100} planes of synthetic lithium fluoride crystals obtained from the Harshaw Chemical Company, Cleveland, Ohio. The crystals were in γ -irradiated condition for the ease of cleaving. The supplier estimated the γ -radiation dose from a ^{60}Co source to be approximately 1.6×10^6 Rontgen. The etchants consisted of an aqueous solution of ferric chloride, with the solution acidified to a standard pH of 1.8. Usually the ferric ion concentration varied from 0 ppm to 10 ppm but some experiments were performed with solutions containing 10 to 1000 ppm.

Cleaving of lithium fluoride was done by putting the crystal in a sample holder. The bulk lithium fluoride was obtained in the shape of a rectangular parallelepiped having the dimensions 30 mm x 5 mm x 5 mm.

All cleavage faces are {100} planes. The cleaving was done by hitting with a small chisel and hammer parallel to {100} plane.

Surface dissolution rates of lithium fluoride cleavages were measured in a Zeiss interference microscope by a "step plate" technique. Portions of the surface were successively protected from the etchant by partially dipping the crystal into a 2% solution of vinyl chloride in methyl ethyl ketone, which produces a plastic coating when dried. The plastic coating was later stripped off when desired. In this way, a successively etched surface was obtained on which a range of dissolution times were represented

when the protective vinyl coating is stripped off and measurements may be made of the step heights at the edge of each time zone. A typical surface arrangement is shown in figure 10a and 10b. Measurements are accomplished with an interference microscope by measuring shifts of fringes as they cross the steps, using thallium green light ($\lambda/2 = 0.27\mu$) for the fractional measurement and employing the zeroth order white light fringe to establish the integral number of fringe shifts. Accurate fringe shifts were determined in terms of fringe spacings on an uninterrupted area by means of a filar micrometer eye-piece (28).

The etching conditions for all the experiments were maintained as constant as possible. About 100 ml of etchant was taken in a beaker and the stirring was done magnetically at a constant rate for all the specimens. All the experiments were done in etchants made from the same stock solution.

Irradiation experiments were done in a Kr-accelerator which is described more in detail below. Radioactive krypton, Kr^{85} , was used for estimating the depth of damage.

Replicas for electron microscopy were of one type - gold-palladium shadowed carbon replicas. This replication technique was already well established in this laboratory. Replicas were removed from the plastic base by floating the samples in a solution of iso-amyl acetate. After times varying from a few hours to a day or two, sufficient dissolution of the plastic base takes place for the replica to float free of the plastic support. The replica was picked up on 200 mesh copper grids and observed in a Phillips EM300 electron microscope. Screen magnification of up to 10,000X to 20,000X were employed in this study - extension to higher

magnifications revealed no additional structure in surfaces replicated by the above technique.

3.2 Bombardment and Counting Techniques

All the irradiations in the present work were carried out using an ion accelerator assembled in our laboratory by Dr. R. Kelly. It was designed to produce heavy gas ions, such as O_2^+ , Kr^+ , Xe^+ etc., at energies up to 45 keV and at currents varying from 1 to 100 μA . This ion accelerator has no mass separation though it permits suppression of secondary electrons. (The lack of mass separation is to some extent compensated by the exclusive use of heavy ions, since impurities would be of low mass, and would create less damage than what one predicts from their abundance.)

Fig. 11 gives the target arrangement and fig. 12 the design of the radio-frequency ion source. In this ion source, the anode (aluminum) is designed to dissipate up to 100 watts of electron energy, and a cathode (nickel) with a 1.5 mm canal allows the extraction of positive ions. The discharge vessel is of pyrex glass and the cathode insulator is sapphire. The purpose of the canal insulator is to shape the plasma boundary, thus causing the emitted ions to be effectively focussed into the cathode entrance (29).

The radio frequency excitation voltage, which is applied externally to the source, originates with an 80 watt, 80 mega-cycle R.F. oscillator. The R.F. field within the coil of the oscillator causes electrons to move from wall to wall with the result that the gas in the ion source is partially ionised (30). In addition, a magnetic coil provides an axial magnetic field of 100 gauss near the extraction canal of the cathode. The magnetic

field is used firstly to intensify the discharge, by increasing the electron path length so that the electrons are used more efficiently; secondly, it pulls the plasma towards the extraction canal.

Below the discharge vessel, there is a series of focussing electrodes with 14 mm holes which are used to regulate the ion beam.

A variable positive focussing potential is applied to the focussing electrodes in accordance with whether a small or large beam is required. Though the exact arrangement of the focussing electrodes is somewhat arbitrary, one normally strives to have the sequence of potentials zero - positive - zero as proposed by Pierce (31). A Faraday cup floating at -850 volts w.r.t. the target is used in order to prevent secondary electrons, which would give current readings too high by a factor of 2 to 3, from leaving the target (an electron leaving the target is electrically indistinguishable from a positive ion striking it). The target is connected to the terminal of a high tension power supply; the particular model used, produced by SAMES (Grenoble), has an internal capacitance of <100 pF and a maximum current of 760 μ A; it thus presents virtually no health hazard.

An important component of the ion accelerator system is the vacuum pump used to evacuate the accelerator column. For this purpose, a 4" oil diffusion pump preceded by a liquid nitrogen trap has been chosen the alternative of ion pumping being unsatisfactory for inert gases. In order to operate properly, the pressure in the accelerated column should be less than 10^{-5} torr, corresponding to a mean free path of greater than 750 cm. If the pressure is higher, the beam will not be properly focussed and will also be contaminated because of scattering from the residual gas molecules.

The radioactive isotope, Kr^{85} , was obtained from Oak Ridge National Laboratory (Oak Ridge, Tennessee).

The amount of radioactive material in each target was measured using a Phillips Scalar and Geiger-Muller probe. The particular G.M. probe had a halogen gas as quenching agent and a mica end-window with a thickness of 3.5 - 4.0 mg/cm^2 . It was thus ideally suited for the 675 keV β -particles emitted by Kr^{85} .

3.3 The Error Estimation

The errors in the experimental measurements chiefly resulted from the measurements of 1) etch time, 2) interference-fringe-shift, 3) irradiation dose and 4) from activity counting and other calculations.

3.3.1 The Etch-Time

Each sample, after etch, was instantaneously dipped in methyl alcohol and dried in ether. Uncertainty in etching time resulted from uncertainties in starting and stopping the etch and amounted to 0.25 sec for each etch.

3.3.2 The Interference Fringe Shift

Accurate fringe shifts were determined in terms of fringe-spacings on an uninterrupted area by means of a filar micrometer eye-piece. Though measurement on the micrometer eye-piece is very accurate but still the error, in this case, is subjective depending from person to person in determining exactly the position of the center of the dark fringe and thus may cause an error of 10% of a fringe. The higher the number of fringe shifts, the less the overall error. Hence the error was estimated to be $\pm 0.03\mu$.

3.3.3 The Irradiation Dose

The error in irradiation dose resulted from 1) the measurement of the ion current, 2) the ion-focussing technique which introduced an uncertainty in the area bombarded and 3) measuring the duration of bombardment.

The error due to this last factor was found to be negligible in comparison to the first two. The error introduced due to all these sources amount to 25% error. But considering the order of the dose, which varied from 10^{13} ions/cm² to 10^{16} ions/cm², this uncertainty in dose in no way affects the results and their interpretation.

3.3.4 Error from Counting and Calculations

It is well known that if N is the number of counts by the G.M. counter, the absolute error is $\pm\sqrt{N}$. Chief error from calculations is faced while normalising the activity versus etch-time curve.

Let,

N_0 = No. of counts at etch-time zero

N_t = No. of counts at etch-time t [for the same surface]

ΔN_0 = Uncertainty in N_0

ΔN_t = Uncertainty in N_t . Then while normalising, we have to

estimate the ratio

$$y = \frac{N_t}{N_0} \quad (3.1)$$

Hence

$$y \pm \Delta y = \frac{N_t \pm \Delta N_t}{N_0 \pm \Delta N_0} \quad (3.2)$$

Δy can be estimated by the usual procedure of error in a quotient such that expanding the expression (3.2) by the Binomial theorem and

taking the suitable limit for errors, Δy can be obtained equal to

$$\frac{\Delta N_t}{N_0} + \frac{\Delta N_0 \cdot N_t}{N_0^2} \quad (3.3)$$

Since $\Delta N_t = \sqrt{N_t}$ (3.4)

$\Delta N_0 = \sqrt{N_0}$ (3.5)

Hence
$$\Delta y = \frac{\sqrt{N_t}}{N_0} + \frac{\sqrt{N_0} \cdot N_t}{N_0^2}$$

$$= \frac{\sqrt{N_t}}{N_0} \left(1 + \frac{\sqrt{N_t}}{\sqrt{N_0}} \right) \quad (3.6)$$

CHAPTER 4
EXPERIMENTAL RESULTS

4.1 A Summary

Results of the experiments basically consist of two parts. In the first part the dissolution rates of the bombarded and non-bombarded surfaces were studied as a function of the ferric-ion concentration in the aqueous solution of ferric chloride. The effect of annealing on the dissolution rate was also investigated.

The second part consists of the studies on the etch-pit formation on bombarded surfaces as a function of the energy of bombardment (5 keV, 15 keV and 35 keV), keeping the ion dose of 10^{16} ions/cm² constant. A study of etch pit formation with the different ion doses of 10^{13} , 10^{14} , 10^{15} and 10^{16} ions/cm² and at a constant energy of 15 keV was also carried out.

The observations of the above two parts were made by investigations on 1) optical microscope, 2) interference microscope and 3) Phillips EM300 electron microscope by replication technique. The results of these experiments are described in detail below.

PART 1

The results of this part are summarised on figures 13 to 18. The experiments represented by figures 13 to 17 were all conducted on the samples bombarded by a 35 keV Krypton ion dose of about 10^{16} ions/cm². Every investigated surface consisted of two parts, half of which was protected by aluminum mask and the other half exposed to the bombarding ions. This

was essential to ensure that the bombarded and shielded surfaces were exactly similar to avoid any discrepancy involved due to even slightly dissimilar surface. The experiments represented by fig. 18 were carried out on samples bombarded by 15 keV Krypton at a dose of 10^{15} ions/cm². The crystal was annealed for 10 minutes at 280°C.

4.2 The Dissolution Experiments

Fig. 13 represents the variation of depth of dissolution with etch time for a 10 ppm ferric chloride solution. Dissolution rate is nearly two times higher on the bombarded surface. In this case etch-time is shorter, hence no further investigations could be done beyond 30 seconds. This is because, at most, only four convenient steps can be formed on a 5 mm long sample. Figure 14 represents the same results as figure 13 except that etch-time interval in the latter is much higher and consisted of 30 sec etch-step and extended up to 120 sec. It is clear from fig. 14 that the dissolution rate during the first 30 seconds on a bombarded surface is nearly two times higher than that on a shielded surface. This is exactly the case in fig. 13. During the interval 30 sec. to 120 sec dissolution rates on both surfaces are the same. This is explained by the fact that radiation damage disappears after about the first 30 seconds etch and after that the etchant does not find any difference between the two surfaces. This explanation is supported by the result of the stripping experiments represented by figure 19A.

Figure 15 represents similar results as figure 14 except that the experiment represented by figure 15 is done with a 2 ppm Fe⁺⁺⁺ solution. The figure can be divided into two parts, the first 15 seconds (A₁) and the latter 45 seconds (A₂). During the first 15 seconds dissolution rate on

the bombarded surface is about 1.5 times higher than that on a shielded surface. During the second part dissolution rates are the same on both surfaces within limits of experimental error. This is explained by the fact that a 2 ppm solution has nearly two times higher dissolution rate than a 10 ppm solution and as a result the radiation damage disappears after 15 sec etch.

Figure 16 represents the experiments conducted on samples etched by distilled water with a standard 1.8 pH and this clearly shows that distilled water i.e. a zero ppm solution does not find any difference between the two surfaces and the dissolution rates are the same on both.

Fig. 17 shows the variation of dissolution rate with Fe^{+++} ion concentration on both bombarded and shielded surfaces. Dissolution rate on the bombarded surface was measured in the region of radian damage. The figure clearly shows the general pattern on shielded surface as reported by Ives and Plewes (28). Here we notice that the difference in dissolution rates between bombarded and shielded surfaces decreases as the ion-concentration decreases and becomes eventually the same at zero ppm ferric ion concentration within experimental errors.

4.3 Effect of Annealing

Figure 18 consists of two curves A and B. Both represent normalised activity versus etch time curves. Activity is normalised with respect to original activity on the sample surface. Curve A is a typical curve (15 keV energy, 10^{15} ions/cm² dose) and with the help of figure 13A it can be used to estimate the activity versus dissolution depth profile on the surface. The figure clearly shows that whereas the unannealed surface takes

about 15 to 20 seconds to remove a depth of about 0.27μ , the annealed surface takes only 10 seconds to remove the depth of radiation damage, which in this case also is about 0.27μ . In other words, the dissolution rate on the annealed (after bombardment) surface is about 1.5 to 2 times higher than that on unannealed (but bombarded) surface. Its explanation is to follow, in the discussion chapter.

Part 2

Part two essentially deals with the investigation of nucleation of etch pits under different experimental conditions. It may further be classified into 1) stripping experiments, 2) optical metallographic observations and 3) replica-electron microscopy.

4.4 Stripping Experiments

Figure 19 represents the normalised activity versus etch time curves. A, B and C represent the samples irradiated with the constant dose of about 10^{16} ions/cm² but at three different ion energies of 35 keV, 15 keV and 5 keV respectively. Nucleation of pits are represented by uncrossed symbols. Crossed symbols signify non-nucleation of pits. Activity is normalised with respect to the original sample activity when the etch time is zero. The sets of figures A, B and C clearly illustrate that the etch pits are visibly nucleated only when the surface is stripped to a critical count rate (i.e. the background count rate).

Figure 20 represents the absolute activity versus etch time curves. The area of all the sample is the same (0.25 cm^2) and the counting is done for 100 seconds. Absolute activity versus the etch-time plot, for the present series, is more informative than the normalised activity versus

etch time curve. The plot symbols have the same meaning as in figure 19. A, B, C and D represent samples bombarded with the same ion energy of 15 keV but different doses of 9.8×10^{15} , 1.2×10^{15} , 1.0×10^{14} and 1.15×10^{13} ions/cm². Experimental errors involved in the experimental series 20 are similar as in 19 but they are not represented on the figure to avoid crowding of the plots.

Curves A and B convincingly demonstrate that for irradiation doses of 10^{15} and 10^{16} ions/cm² nucleation of etch pits takes place only when the radiation damaged region is completely stripped. But this is not so in the case of curves C and D. Curves C and D represent the ion doses of 1.0×10^{14} and 1.15×10^{13} ions/cm² when pitting takes place well above the background activity level, or more quantitatively even at a fraction of about 0.5 of the original activity. Actually it was noticed carefully that nucleation of pits for the curves C and D took place nearly simultaneously on the bombarded as well as unbombarded surfaces with the one difference that the pits on the bombarded surfaces were smaller in dimensions than those on non-bombarded surfaces.

Fig. 21 represents the experiments performed with different Fe⁺⁺⁺ ion concentrations on four samples irradiated with a constant dose of about 10^{15} ions/cm² and at a constant energy of 15 keV. It is demonstrated from the curves that as far as the nucleation of pits was concerned, ion concentration in the solution did not play any significant role. Nucleation of pits was neither retarded nor accelerated by ion concentration which extended from 10 ppm onward to 1000 ppm. In all the cases, the nucleation of pits took place only when the radiation damage is stripped from the sample.

4.5 Optical Metallographic Observations

Figures 22 to 30 represent the results obtained from the metallography experiments. Figures 22 and 23 represent the first and second etching steps of the sample irradiated at a dose of about 10^{16} ions/cm² and at an energy of 35 keV. Figure 22 consists essentially of three parts A, B and C. A is unetched. B and C are etched for 30 seconds in a 10 ppm solution, hence a dissolution step is formed between A on the one hand and B and C on the other. Moreover, B is irradiated but C is shielded with an aluminum cover. We see etch pits on C but none on B. Figure 23 represents a second dissolution step of the same sample. It has four segments A, B, C and D. There is a dissolution step between A and B on one hand and C and D on the other. A and B of fig. 23 represent the same surfaces as B and C of fig. 22 respectively. A and C represent irradiated regions of the same sample but B and D shielded. A and B of fig. 23 are etched for 30 seconds in the same way as B and C of fig. 22. C and D of fig. 23 both are etched for 60 seconds.

We see no pits on A, pits on B, C as well as D. Pits on D are much bigger than those on B, which is natural. Similarly pits on D are much bigger than those on C. Figure 23 shows that pitting on bombarded surface takes place between an etch of 30 sec to an etch of 60 sec. Considering the relatively equal sizes of pits on B and C, we conclude that pitting on C might have taken place after 30 secs of etch treatment. Checking with the activity versus etch-time profile of figure 19A, we conclude that pitting has taken place when the activity, which represents the radiation damage, is very near the background level i.e. when the radiation damage is removed.

Figure 24 represents experiments performed on the upper face of a sample bombarded with an ion energy of 15 keV and at an ion dose of 10^{15} ions/cm². Ion energy plays a role only on increasing or decreasing the depth of radiation damage. Fig. 24 has two segments A and B etched for 5 seconds and 25 seconds respectively. A has no pits. B shows well developed pits. Fig. 25 is the lower and opposite face of the same sample and is self-shielded. A and B are similarly etched for 5 and 25 seconds as in the case of segments A and B of figure 23. These two figures show that shielded surface A of fig. 25 does give etch pits but irradiated surface A of fig. 24, which is also similarly etch treated, does not.

Fig. 26 shows the experiment performed on a sample bombarded with an ion dose of 10^{14} ions/cm² and at an energy of 15 keV. A is the unetched surface; B is etched for 3 seconds. This figure shows that at a low dose of 10^{14} ions/cm², even the irradiated surface does give etch pits in contrast to the results of fig. 24 and 25. This favourably compares with the results of fig. 20 or rather confirms it.

Figures 27, 28, 29 and 30 represent the experiments performed on the interference microscope. Figures 27 and 28 are exactly the same areas on the same samples as figures 22 and 23. We see that neither the segment B of fig. 27 nor the segment A of fig. 28 show any pitting structures. These two confirm the results obtained on figure 22 and 23.

Figure 29 and 30 are exactly the same areas as figures 24 and 25 and all the experimental results for all the segments are the same, with the only difference that figures 29 and 30 are taken on the interference microscope. Results of figures 29 and 30 confirm the results of figures 24 and 25.

4.6 Replica-Electron Microscopy

Figures 31, 32 and 33 summarise the results obtained on the electron microscope. The sub-figures A, B, C and D of figure 31 represent segment B of fig. 22 or segment A of figure 23 at magnification ranging from 2,500X to 22,500X. These figures show just rough surfaces uniformly etched without any points of preferential attack, which are necessary for the formation of well-defined pits.

Figure 32 shows a sample bombarded at a dose of 10^{15} ions/cm² and at an ion energy of 15 keV. A represents a junction of the bombarded surface after 5 sec and 25 sec etch at 2,500X. B represents the same junction at 7,500X. C and D represent the bombarded surface after 5 sec etch and at a magnification of 10,000X and 22,500X. Surfaces C and D are rough and present no evidence for the formation of etch-pit nuclei.

Fig. 33 represents a sequence of etching experiments performed on a sample bombarded with 10^{15} ions/cm² dose at an ion energy of 15 keV. The sub-figures A, B, C, D and E represent the surfaces after 0, 5, 10, 15 and 20 seconds etch at a magnification of 5×10^3 . The "dots" on D and E are due to some experimental error and are non-reproducible. A is just the bombarded surface without etch. B has a rough surface after 5 sec etch - (no pits). After 10 sec etch the surface of C is smoother than that of B - (still no pits). Sub-figure D shows the initiation of pits (the arrows show it). In sub-figure E, pits are developed.

CHAPTER 5
A DISCUSSION

In the last chapter we dealt with the experimental results. To facilitate the discussion in the present chapter it is convenient to classify it into two parts. The first part will deal with the dissolution experiments and the second with the studies on radiation damage and the nucleation of pits.

5.1 On the Dissolution Experiments

We have chiefly two observations on the dissolution experiments. Firstly, the bombarded surface has a higher dissolution rate than the non-bombarded surface. Secondly, a bombarded and annealed surface has a much higher dissolution rate than a bombarded surface under similar etching conditions.

When LiF is irradiated with Krypton, 1) kink-density along a ledge as well as 2) the thermodynamic potential of the bombarded region of the crystal is increased. Increase in the thermodynamic potential is caused because of the transfer of energy from the bombarding particles to the constituent atoms of the crystal. As a result, the dissolution rate in principle increases.

A model of two types of kinks in a surface ledge is shown in fig. 3. Filled circles show the adsorption of inhibitor ions. Gilman, Johnston and Sears (14) have suggested that the most suitable site for the incorporation of Fe^{+++} ions into a lithium fluoride surface would be at kink positions where they could be surrounded by neighboring F^- ions of the

crystal (as at B in fig. 3). Ives and Baskin (15), though, have preferred to consider the A kink-pairs as the principal sites for adsorption. The role of the inhibitor ions is to hold up the inhibited kinks and the kinks will not be able to traverse their ledges or get annihilated by kinks of opposite sign. By increasing the density of kink sites due to ion bombardment, one is increasing the density of inhibition sites. Due to contribution due to increased ion inhibition the dissolution rate should decrease. This leads us to believe that if the kinks are the only dissolution sites, then all the kinks are not inhibited or some of the kinks might be such that they are surrounded by Li^+ ions of the crystal where Fe^{+++} cannot inhibit due to electrostatic repulsion. As a result, the higher dissolution due to increase in thermodynamic potential increases. Moreover, it might be proposed that because of transfer of energy from the bombarding particles to the constituent atoms of the crystal, the binding energy of the atoms around the kink site is sufficiently weak so that even though the Fe^{+++} ion is adsorbed at the kink site it is not in a position to efficiently inhibit dissolution at that point.

Secondly, it has also been observed that the bombarded and annealed surface has a much higher dissolution rate than a bombarded surface. Annealing in our experiment was performed at 280°C for 10 minutes. This could be explained by the fact that during annealing many vacancies cluster together and give rise to distinct cavities and hence the densities of cavities after annealing is higher than that before annealing. As a result the average distance between two cavities decreases. Furthermore, cavities (as well as defect clusters due to aggregated Frenkel defects) can be

regarded as primary dissolution sites and the rate of dissolution is a function of the average distance between cavities or aggregated Frenkel defects. The smaller the distance, the higher the dissolution rate. This might explain the observed higher dissolution rate on a bombarded and annealed surface. Individual vacancies are expected much less to contribute for the nucleation of dissolution sites. This is because the strain energy associated with a cavity is much higher than that associated with an individual vacancy. Though the average free energy of the specimen decreases due to coalescence of a number of vacancies, the larger strain energy associated with a cavity makes it a site for preferential dissolution.

5.2 On the Stripping Experiments

On the stripping experiments we have observed that an ion dose of 10^{13} or 10^{14} ions/cm² for a given energy of 15 keV gives rise to etch-pitting but not the ion dose of 10^{15} or 10^{16} ions/cm². We can discuss this phenomenon approaching macroscopically and then microscopically.

5.2.1 A Macroscopic Approach

To understand the role of radiation damage on the development of pits, let D and N be a dislocation and a non-dislocation site on the crystal surface. Let V_d (fig. 34) be the dissolution rate at D and V_n at N. Therefore to observe a pit at D, we must have

$$V_d > V_n \quad (5.1)$$

This relation is satisfied for a non-bombarded sample. Since the pitting does not take place for a bombardment dose of 10^{15} and 10^{16} ions/cm² it leads us to the conclusion that at this radiation dose

$$V_{dB} \approx V_{nB} \quad (5.2)$$

where V_{dB} = Dissolution rate at a dislocation on a bombarded sample

V_{nB} = Same at a non-dislocation site on a bombarded sample

Let μ_{dn} = Chemical potential at a dislocation on a non-bombarded surface

μ_{nn} = Chemical potential at a non-dislocation site on a non-bombarded surface

$\Delta\mu$ = Increase in chemical potential due to nearly uniform bombardment everywhere for an unbombarded surface.

$\mu_{dn} > \mu_{nn}$ gives rise to $V_d > V_n$ which explains the formation of pits on a non-bombarded surface. But for a bombarded surface, total chemical potential at a dislocation is

$$= \mu_{dn} + \Delta\mu \quad (5.3)$$

Similarly, total chemical potential at a non-dislocation site is

$$= \mu_{nn} + \Delta\mu \quad (5.4)$$

Therefore for formation of pits

$$\mu_{dn} + \Delta\mu > \mu_{nn} + \Delta\mu \quad (5.5)$$

This is true, but in my opinion, for the dose of 10^{15} and 10^{16} ions/cm²

$$\Delta\mu \gg \mu_{dn} \text{ or } \mu_{nn}$$

then

$$\mu_{dn} + \Delta\mu \approx \mu_{nn} + \Delta\mu \quad (5.6)$$

Hence we do not observe pits. For a dose of 10^{13} and 10^{14} ions/cm², $\Delta\mu$ is not much greater than μ_{dn} or μ_{nn} , hence it does satisfy the inequality

$$\mu_{dn} + \Delta\mu > \mu_{nn} + \Delta\mu \quad (5.7)$$

within experimental results.

From this discussion we conclude that at a bombardment dose of 10^{15} or 10^{16} ions the energy imparted to the constituent atoms of the crystal are so significant that nearly all the atoms are nearly equally weakly bound. As a result, no special notice of the atoms at the dislocation site is taken of.

5.2.2 The Microscopic Approach

Let V_s represent the mean velocity of movements of steps by removal of atoms

Let λ_0 (fig. 35) be the distance between two nucleation sites on a defect-free surface. Then time taken to travel a distance λ_0 for the dissolving surface

$$= t_0 = \frac{\lambda_0}{2V_s} \quad (5.8)$$

If h is the step height at the surface, then V_n/h steps are developed per unit time. Then for a uniform dissolution, time for removal of steps on the surface must be smaller than the time for the formation of a step. Hence

$$\frac{\lambda_0}{2V_s} < \frac{h}{V_n} \quad (5.9)$$

V_s and V_d are microscopic quantities and can, therefore, be considered unaffected by radiation damage. Inequality (9) can be further written as

$$\lambda_0 < 2h \cdot \frac{V_s}{V_n} \quad (5.10)$$

for uniform dissolution everywhere.

When pitting is just observed, though $V_d \gtrsim V_n$, it may be taken as

$$V_d \approx V_n \quad (5.11)$$

for calculation purposes.

Ives and McAusland (32) have reported pit slope for LiF etched in aqueous solution of FeCl_3 .

$$\text{For LiF, } \frac{V_d}{V_s} = \frac{V_n}{V_s} \approx 0.1 \quad (5.12)$$

Putting the value (5.12) in (5.10)

$$\begin{aligned} \lambda_0 &< 2h \cdot \frac{1}{0.1} \\ \text{or } \lambda_0 &< 20 h \end{aligned} \quad (5.13)$$

Since step heights in LiF are monomolecular $h \approx 4\text{\AA}$

$$\text{then } \lambda_0 < 80\text{\AA} \quad (5.14)$$

Relation (5.14) puts an upper limit for λ_0 i.e. nucleation sites for dissolution.

Experimentally there is an etch pitting for a dose of 10^{14} ions/cm². This dose gives an average distribution of one ion/100 \AA^2 which gives the average distance between two ion-impact sites to be of the order of 10\AA . But $10\text{\AA} < \lambda_0$. Hence it is not reasonable to assume that each ion impact forms a nucleus for dissolution. Because in that case even for a dose of 10^{14} ions/cm² there should be uniform dissolution according to the above analysis which requires a distance of less than 80\AA between two dissolution nuclei for uniform dissolution. This confirms the observations of Gilman and Johnston (25) which state that rough etching is not caused by individual point defects but by aggregates of defects. Therefore λ_0 represents the distance between the aggregates of defects which leads us to conclude that an ion dose of 10^{14} ions/cm² creates aggregates of defects such that distance between two aggregates of defects is always greater than 80\AA whereas a

dose of 10^{15} ions/cm² increases the density of such aggregates such that average distance between two aggregates of defects is lower than 80\AA and hence the rough etching.

5.2.3 Fe⁺⁺⁺ Ion Concentration and Nucleation of Pits

It has been observed that as far as the nucleation of pits is concerned 10 ppm, 100 ppm, 500 ppm and 1000 ppm of Fe⁺⁺⁺ ion concentration do not make any noticeable difference. This is because of the fact that dissolution rate due to all these ion concentrations in the solutions is nearly the same. As a result they take the same time for stripping the damaged layers.

REFERENCES

1. W. K. Burton, N. Cabrera and F. C. Frank, Phil. Trans. Roy. Soc. 243A, 299 (1951).
2. F. C. Frank, "Growth and Perfection of Crystals", Edited by R. H. Doremus, B. W. Roberts and D. Turnbull (John Wiley and Sons, New York, 1958), p. 411.
3. N. Cabrera and D. A. Vermilyea, Reference (2), p. 393.
4. A. A. Chernov, Dokl. Akad. Nauk S.S.R. 117, 983 (1957).
5. W. Kossel, Nach. Ges. Wiss. Gottingen, 135 (1927).
6. I. N. Stranski, Z. Physik. Chem. 136, 259 (1928); 11, 421 (1931).
7. J. Frenkel, J. Phys. U.S.S.R. 9, 392 (1945).
8. W. K. Burton and N. Cabrera, Discussions Faraday Soc. 5, 33 (1949).
9. J. P. Hirth and G. M. Pound, J. Chem. Phys. 26, 1216 (1957).
10. A. H. Cottrell, "Dislocations and Plastic Flow in Crystals" (Oxford University Press, Oxford, 1953), p. 38.
11. N. Cabrera and M. M. Levine, Phil. Mag. 1, 450 (1956).
12. N. Cabrera, M. M. Levine and J. S. Plaskett, Phys. Rev. 96, 1153 (1954).
13. N. Cabrera, "Semiconductor Surface Physics". Edited by R. H. Kingston (University of Pennsylvania Press, Philadelphia, 1957), p. 327.
14. J. J. Gilman, W. G. Johnston, G. W. Sears, J. Appl. Phys. 29, 747 (1958).
15. M. B. Ives and M. S. Baskin, J. Appl. Phys. 36, 2057 (1965).
16. M. W. Thomson, "Defects and Radiation Damage in Metals" (Cambridge at the University Press, 1969) p. 52.
17. J. Frenkel, Zeits. Physik, 35, 652 (1926).

18. C. Wagner and W. Schottky, Z. Phys. Chem. (B) 11, 163, 1930.
19. W. Schottky, Naturwissen. 23, 656 (1935); Z. Phys. Chem. (B) 29, 335 (1935).
20. F. Seitz, Revs. Mod. Phys. 18, 384 (1946) and 26, 7 (1954).
21. J. Washburn and J. Nadeau, Acta Met. 6, 665 (1958).
22. J. J. Gilman and W. G. Johnston, "Solid State Physics - Advances in research and applications, vol. 13", Edited by F. Seitz and D. Turnbull (Academic Press, New York and London, 1962), p. 162.
23. J. J. Gilman, Acta Met. 7, 608 (1959).
24. H. B. Huntington, J. E. Dickey, and R. Thomson, Phys. Review, 100, 1117 (1955).
25. J. J. Gilman and W. G. Johnston, J. Appl. Phys. 29, 877 (1958).
26. M. Lambert and A. Guiner, Compt. rend. Acad. Sci. 244, 2791 (1957); 245, 526 (1957).
27. D. A. Young, Nature 182, 375 (1958).
28. M. B. Ives and J. T. Plewes, Journal of Chem. Phys. 42, 293 (1965).
29. D. D. Moak, H. Reese and W. M. Good; Nucleonics 9, 18 (1951).
30. V. M. Fetz and O. Oechsner, Zeit Angew. Phys. 12, 250 (1960).
31. J. R. Pierce, Theory and Design of Electron Beams, Van Nostrand (1954).
32. M. B. Ives and D. D. McAusland, Surface Science 12, 189 (1968).

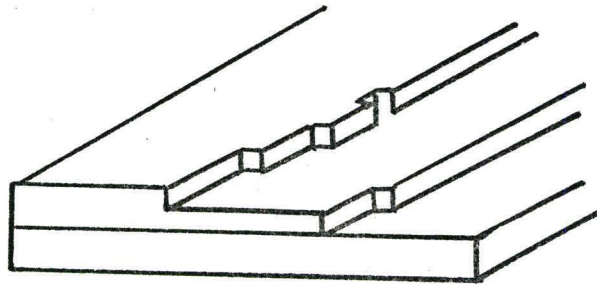


Fig. 1 Kossel model of a crystal surface showing close packed $\{100\}$ surface, ledges and kinks.

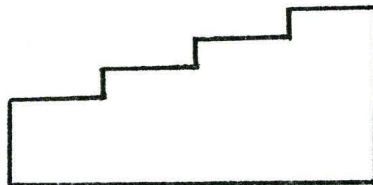


Fig. 2 Two dimensional model of a general surface represented by an array of ledges.



Fig. 3 Two types of kinks in a surface ledge which may be hosts to inhibitor ions (filled circles).

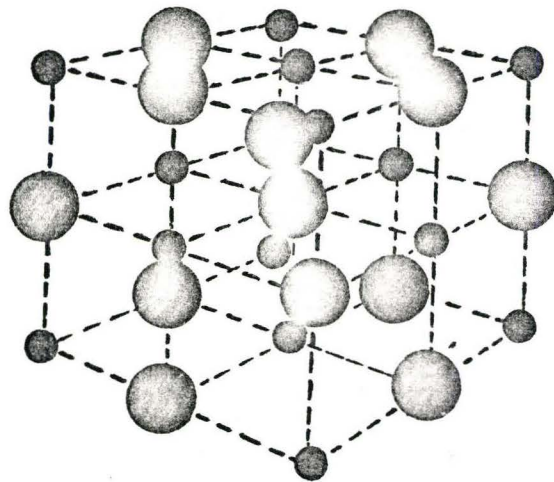


Fig. 4 The lithium fluoride crystal structure. The space lattice is fcc, and the basis has one Li^+ ion at $0, 0, 0$ and one F^- ion at $1/2, 1/2, 1/2$.

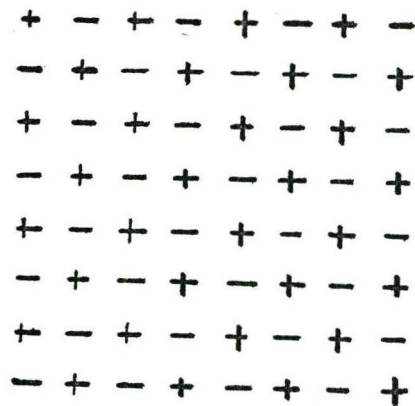


Fig. 5 Two dimensional perfect crystal.

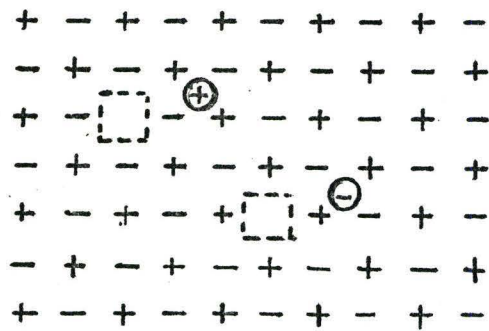


Fig. 6 Frenkel defects (interstitial cations and anions with corresponding vacancies).

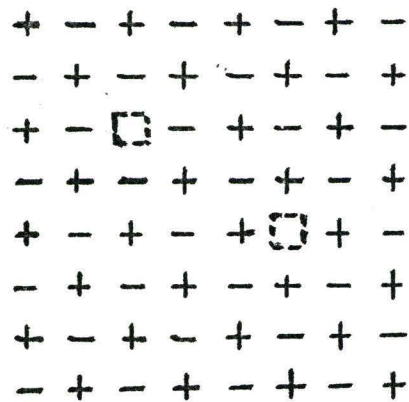


Fig. 7 Schottky defect (cation and anion vacancies).

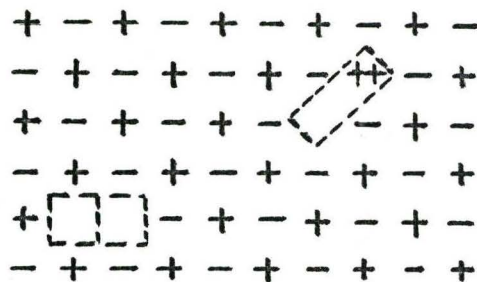


Fig. 8 Vacancy pair and divalent ion-vacancy complex in lithium fluoride.

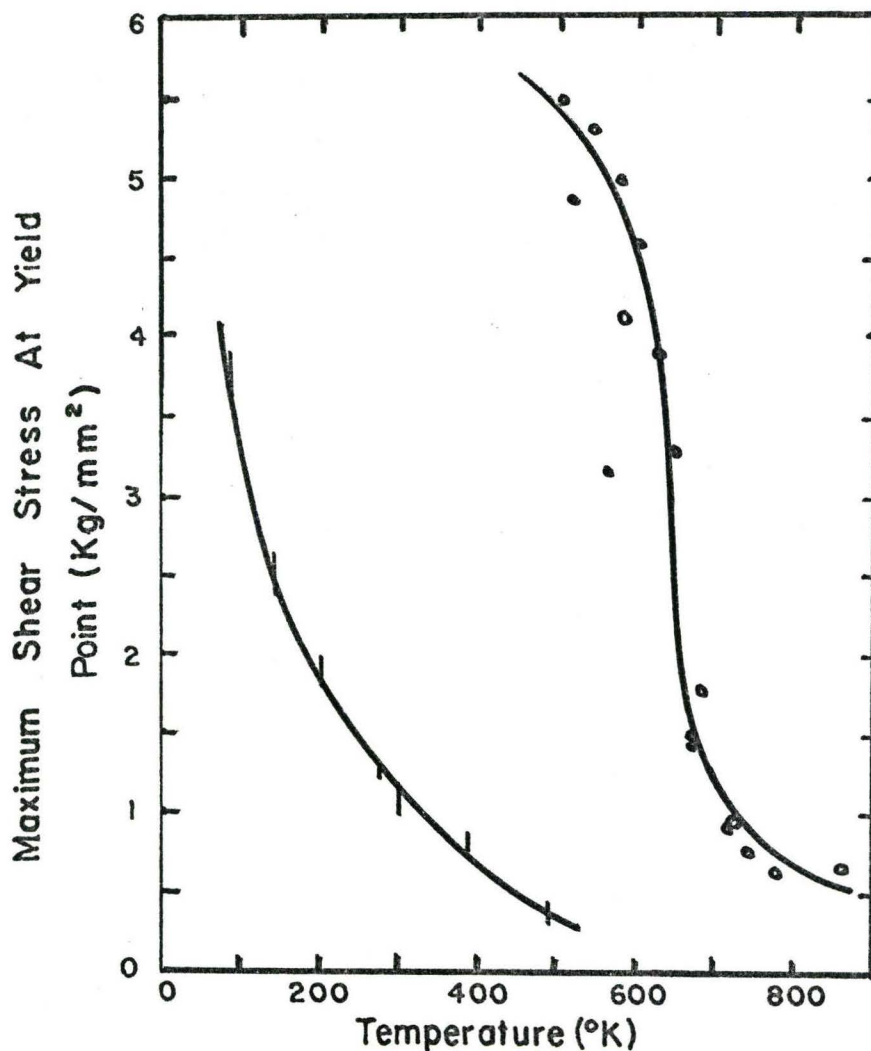


Fig. 9 Comparison of stress for (100) glide with stress for (110) glide in LiF crystals.
(Reproduced from J.J. Gilman, *Acta Met.* 7, 608 (1959)).

10A

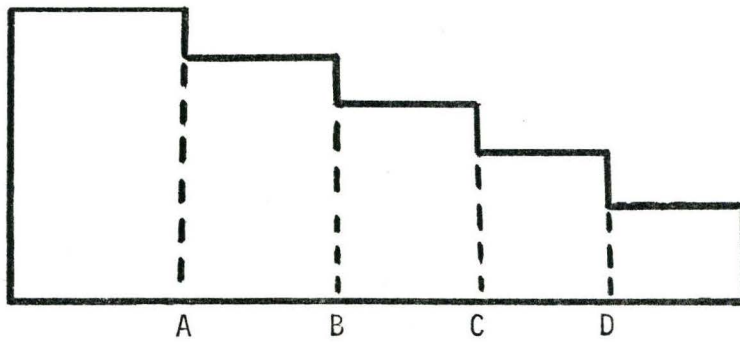
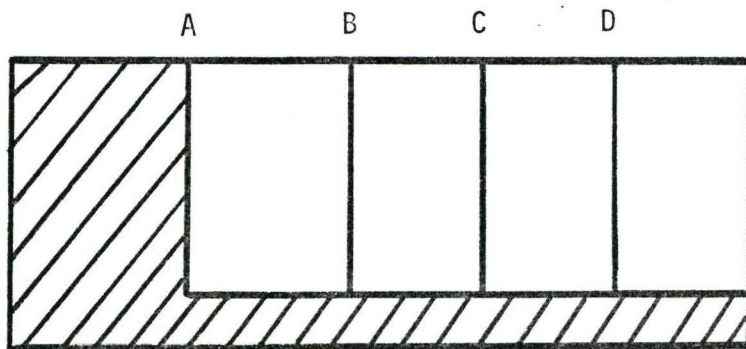


Fig. 10 A typical surface arrangement after etching.

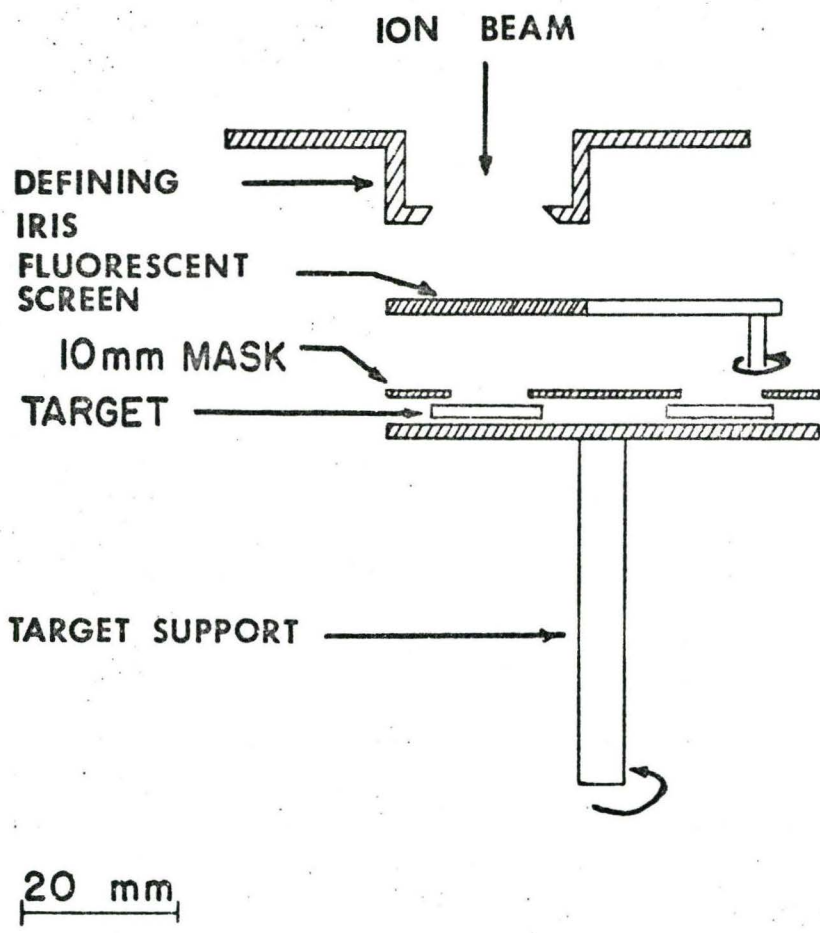
A) Side view

B) Top view

10B



(Dashed region is shielded). A,B,C,D are four etched steps.



Target Arrangement

Fig. 11

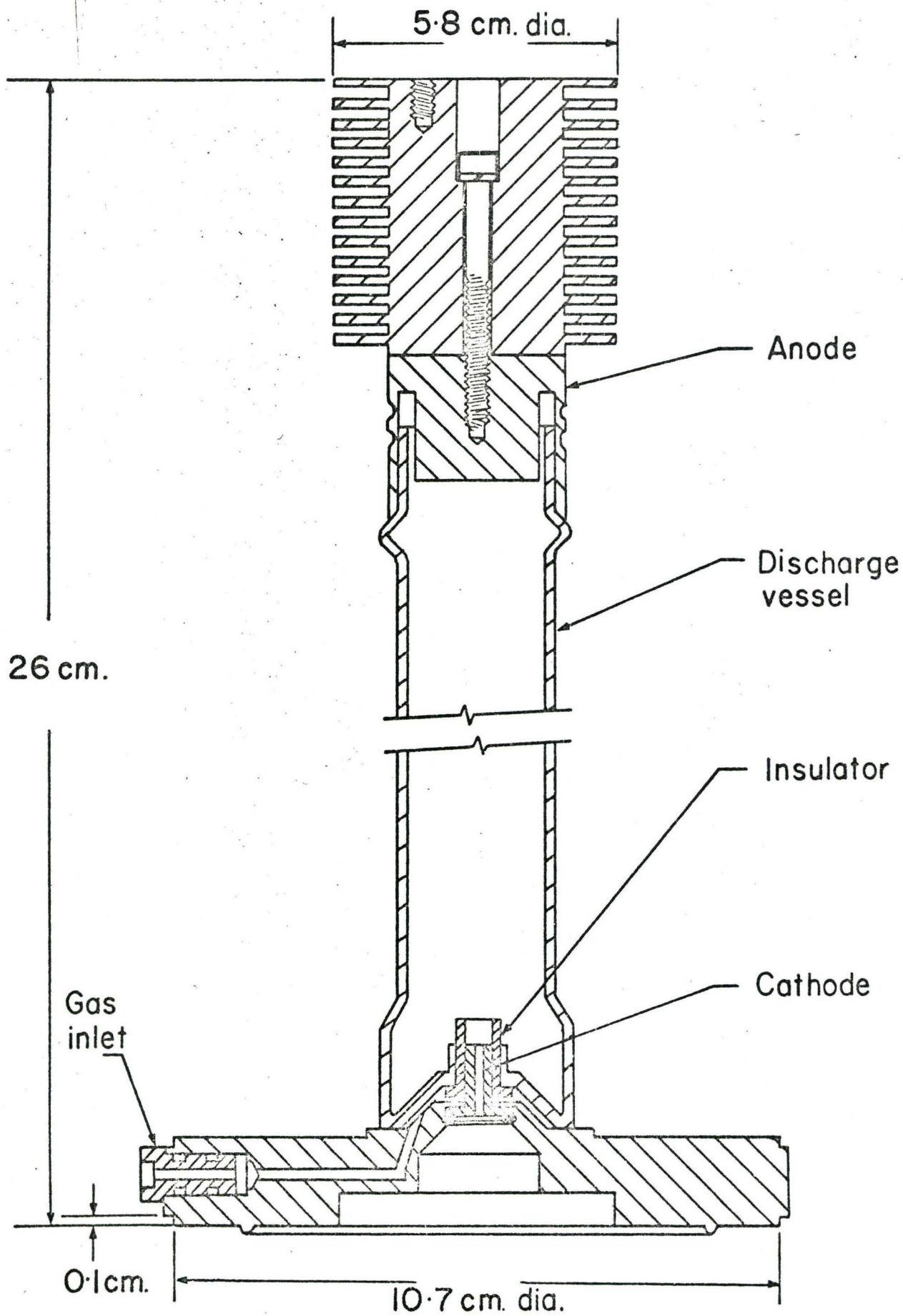


Fig. 12 The Ion Source

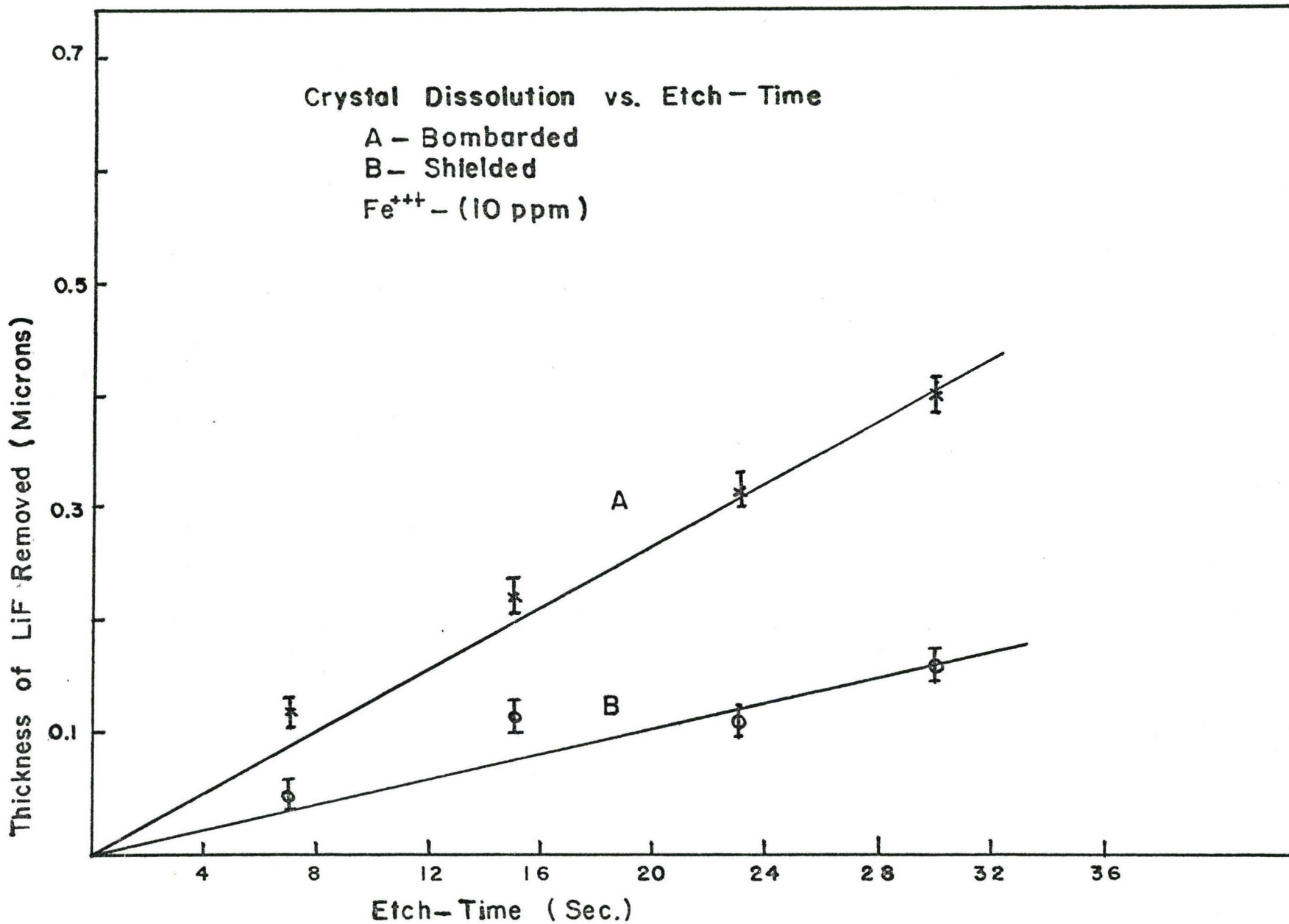


Figure 13

Crystal Dissolution vs. Etch-Time

A-Bombarded

B-Shielded

Fe⁺⁺⁺- (10 ppm)

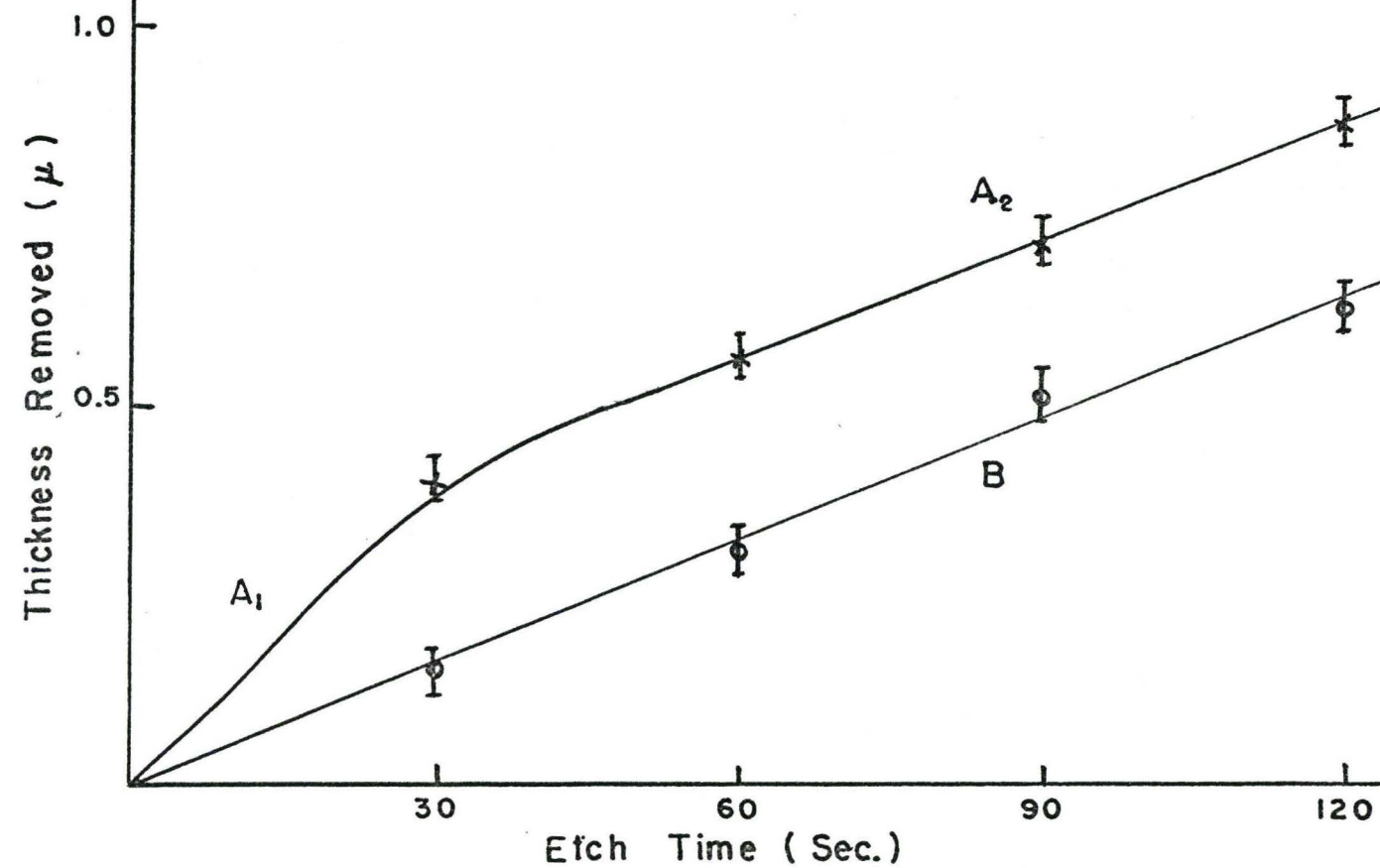


Figure 14

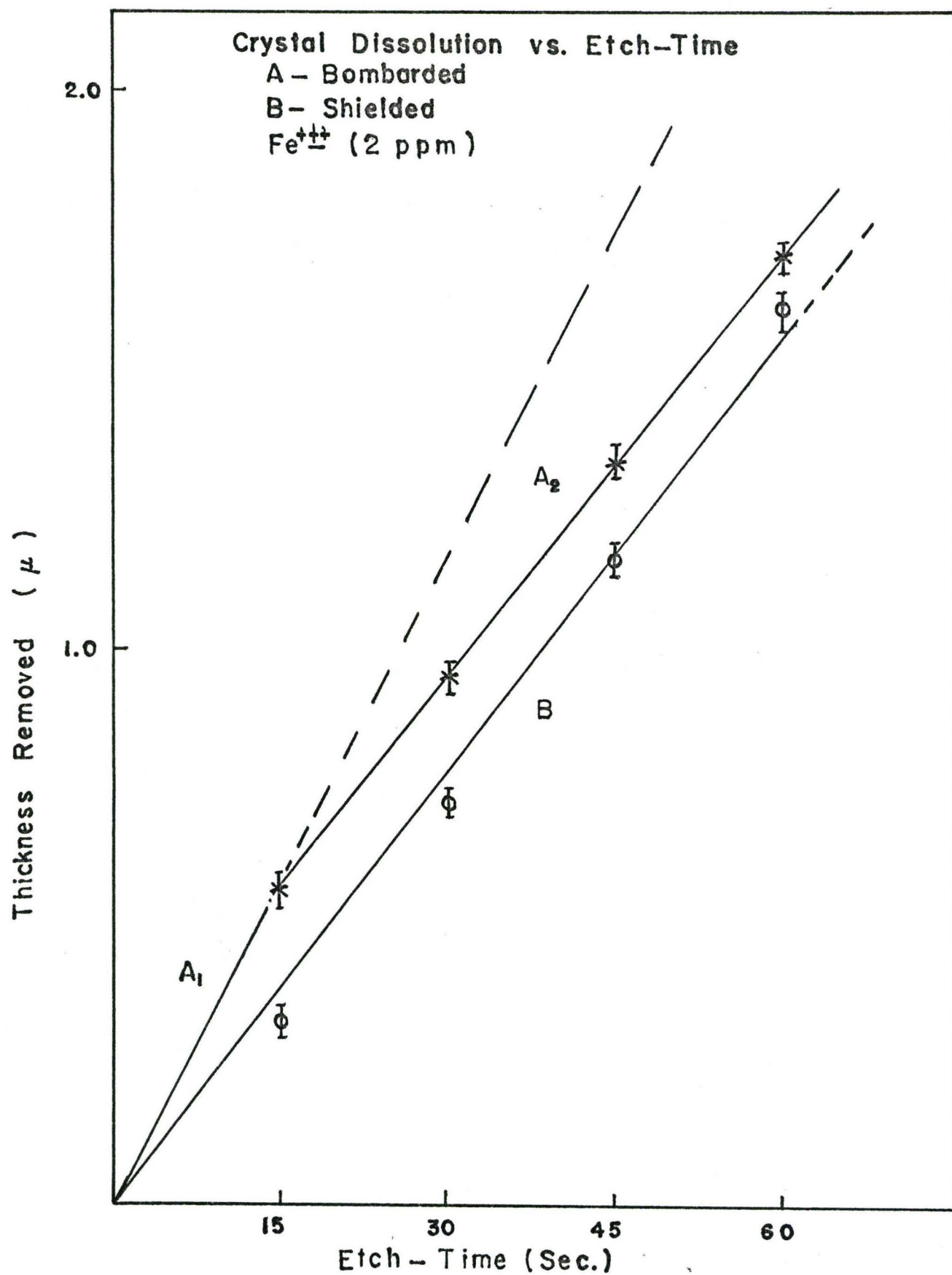


Figure 15

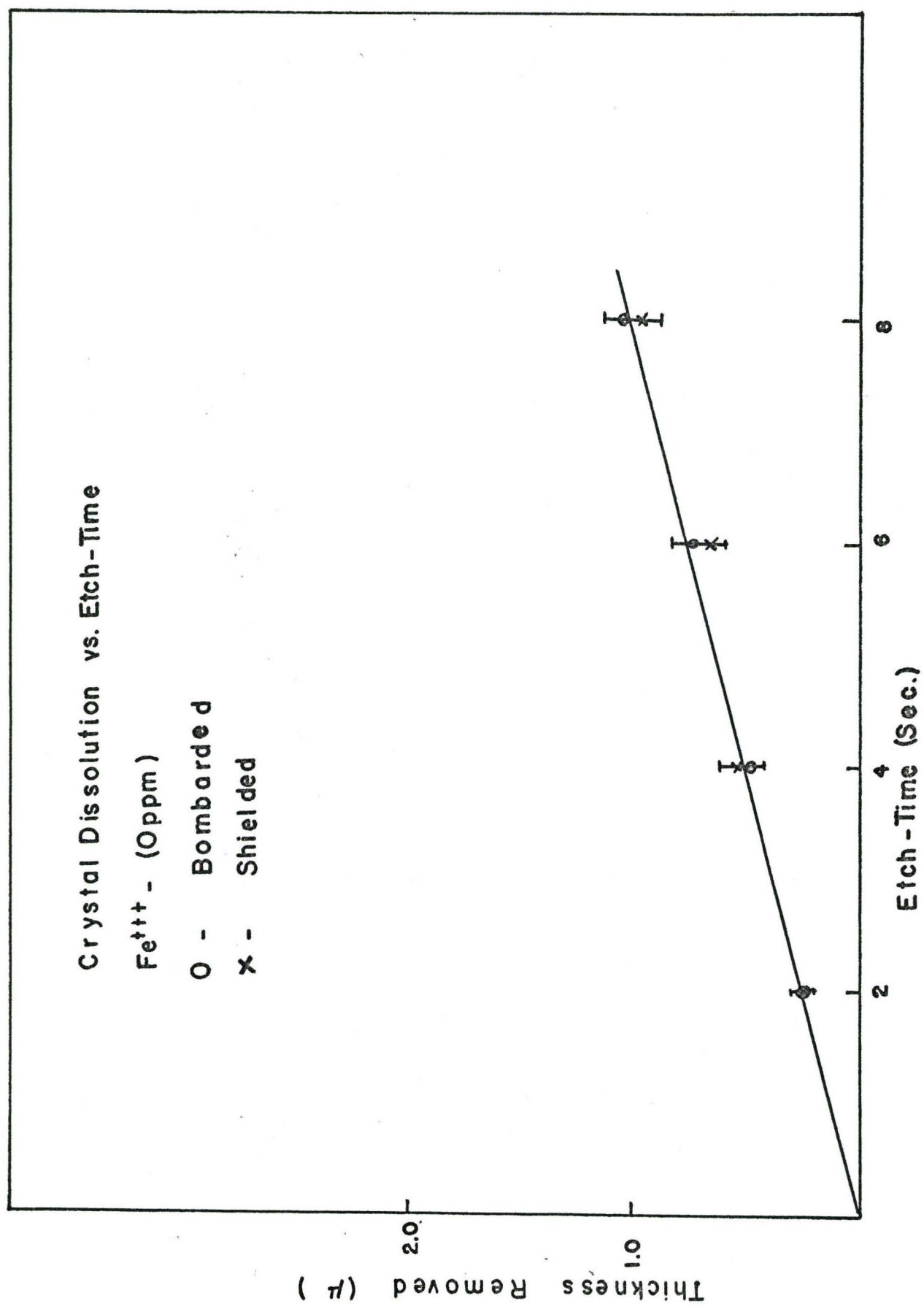


Figure 16

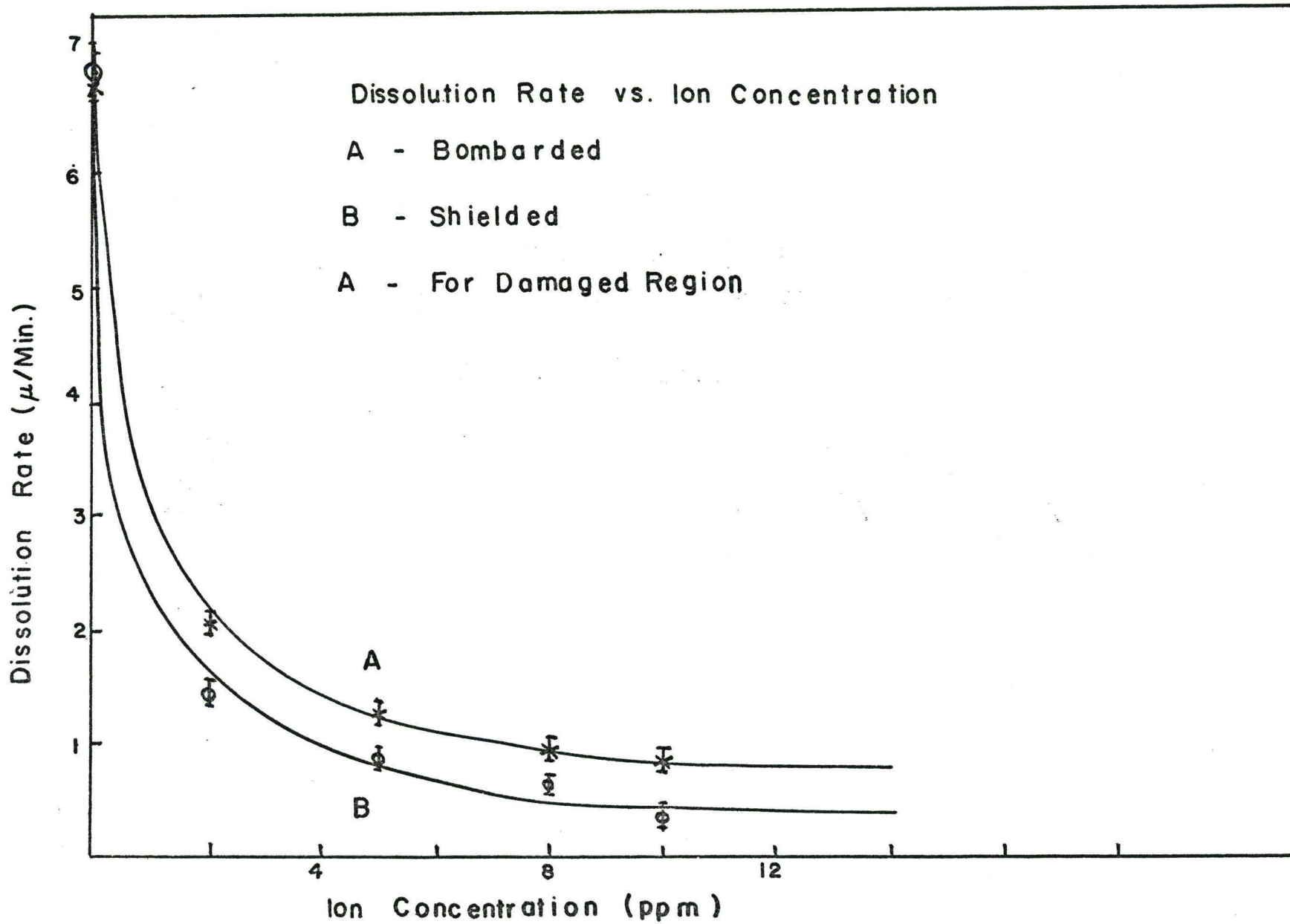


Figure 17

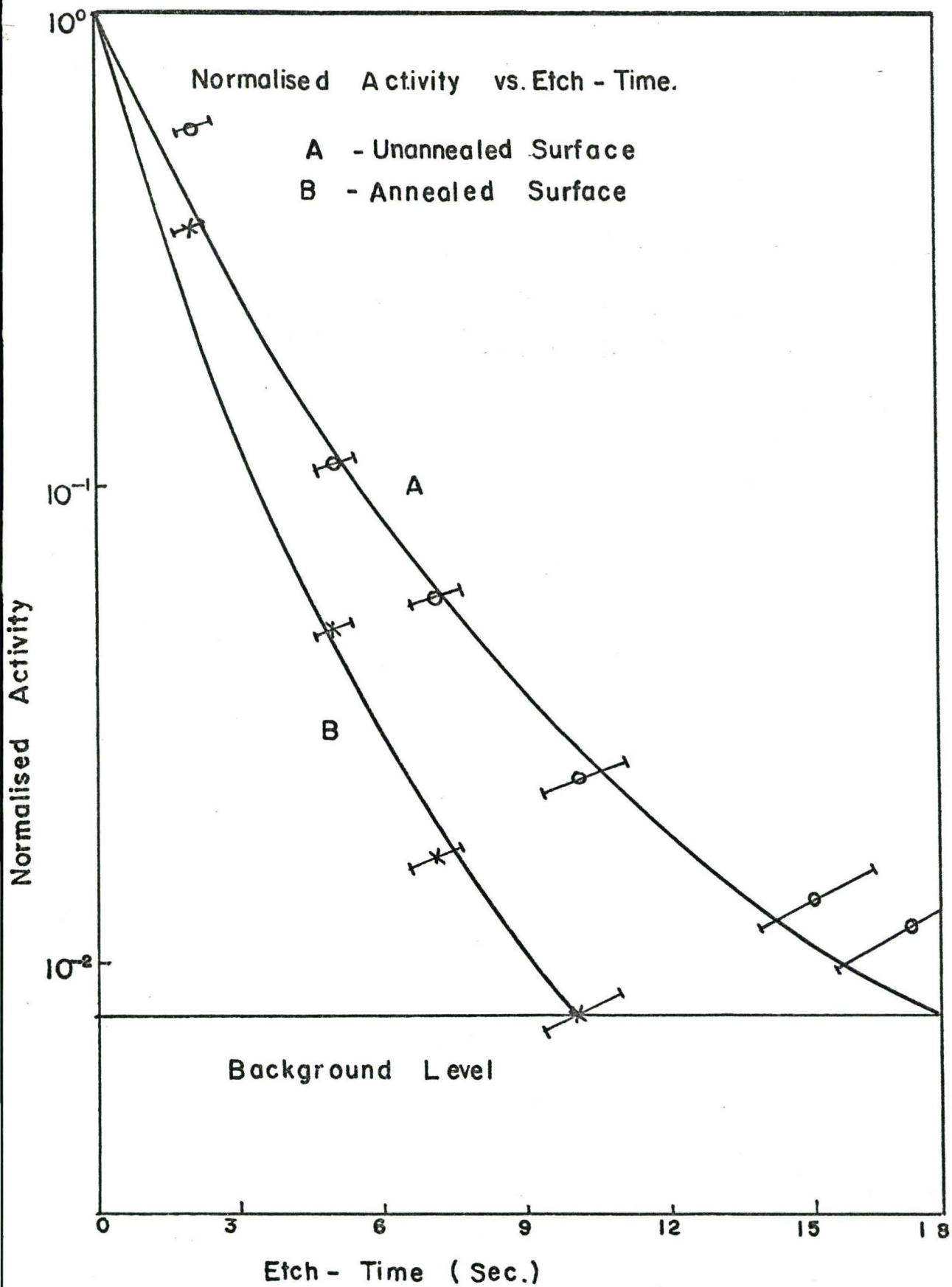


Figure 18

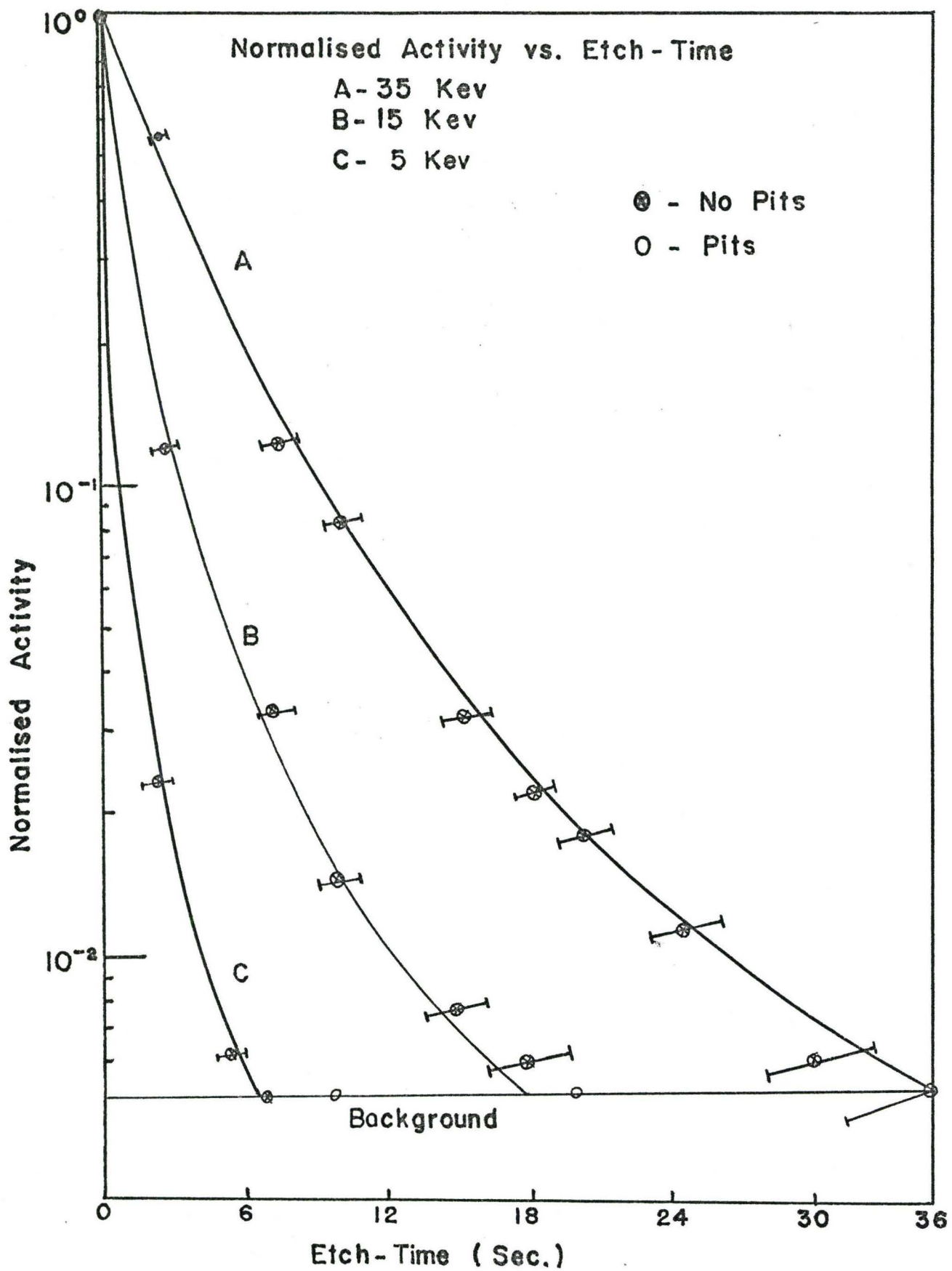


Figure 19

Absolute Activity vs. Etch-Time

Legends $\otimes, \diamond, \boxplus, \triangle$ - No Pits

$\circ, \diamond, \square, \triangle$ - Pits

Doses A - 10^{16} ions/cm²

B - 10^{15} "

C - 10^{14} "

D - 10^{13} "

Energy - 15 Kev

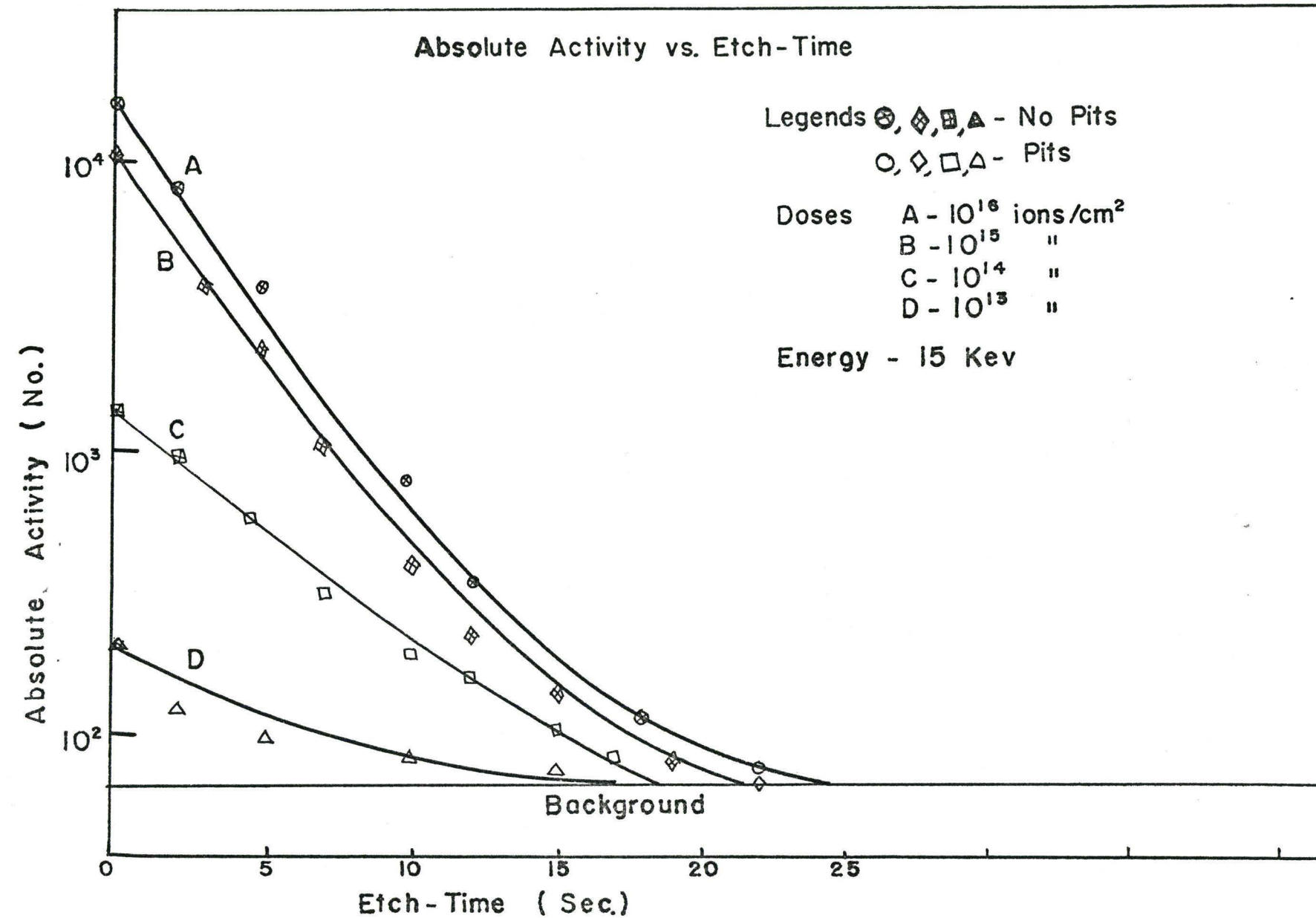


Figure 20

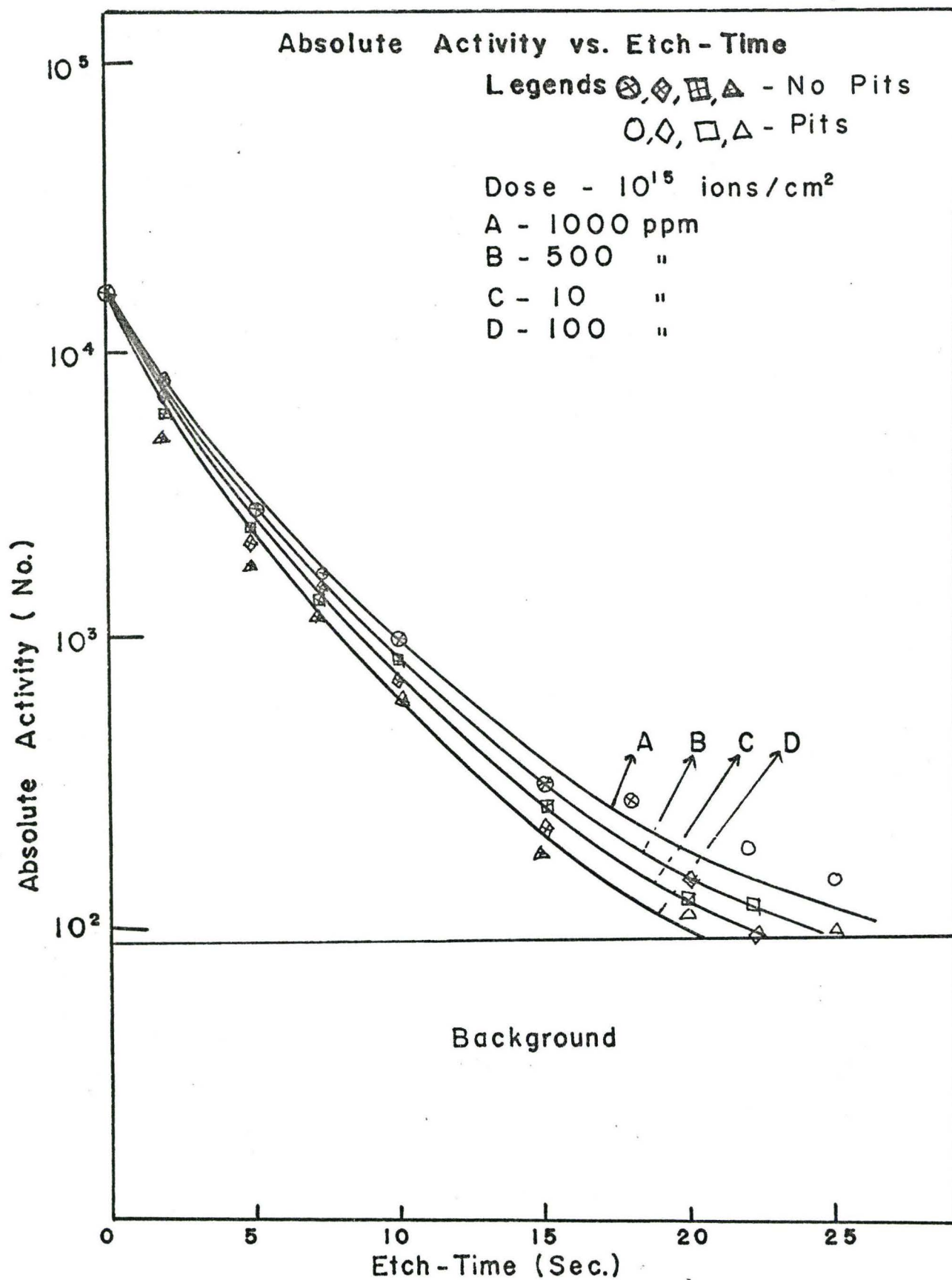


Figure 21

Fig. 22

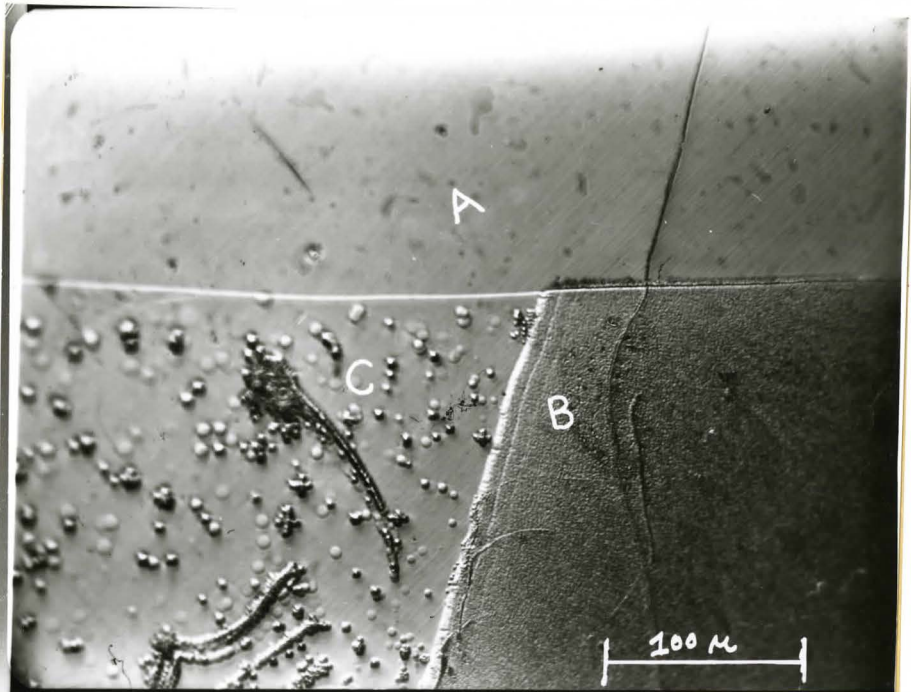


Fig. 23

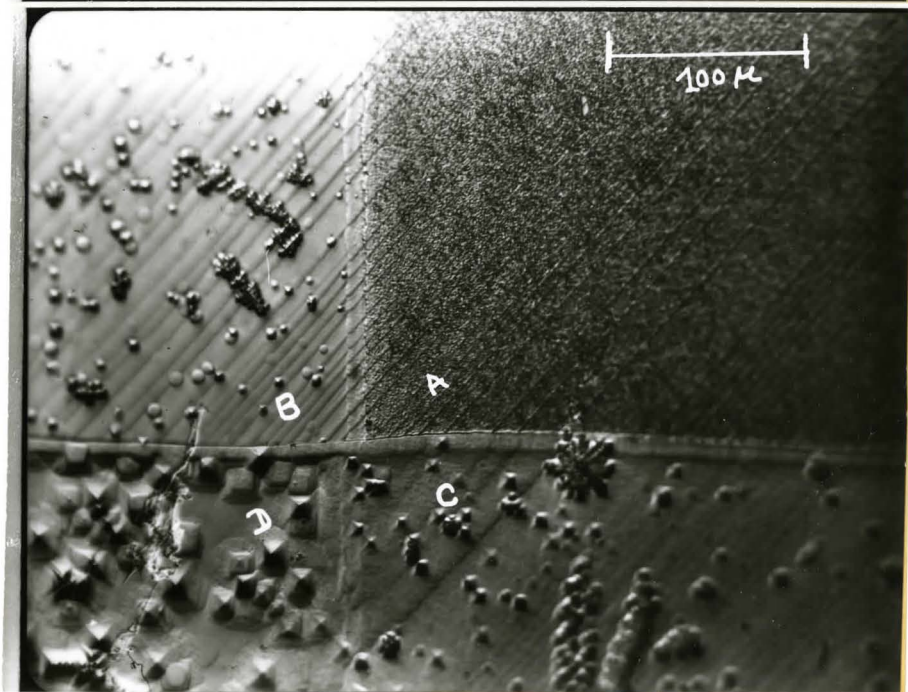


Fig. 22 Figure represents three regions A, B, C at 256X (see text).

Fig. 23 Figure represents four regions A, B, C, and D at 256X (see text).

Fig. 24

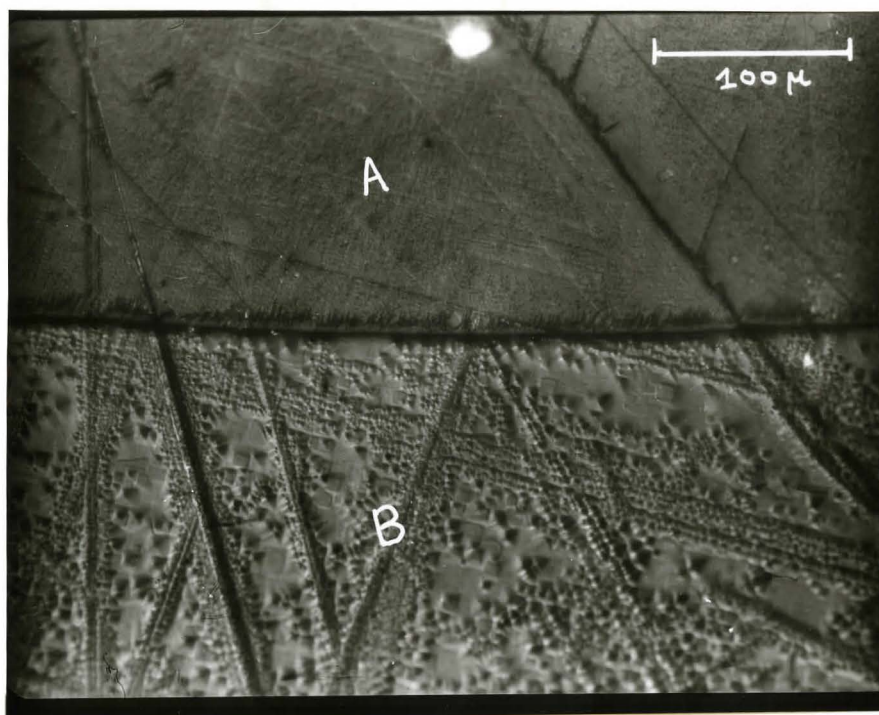


Fig. 25

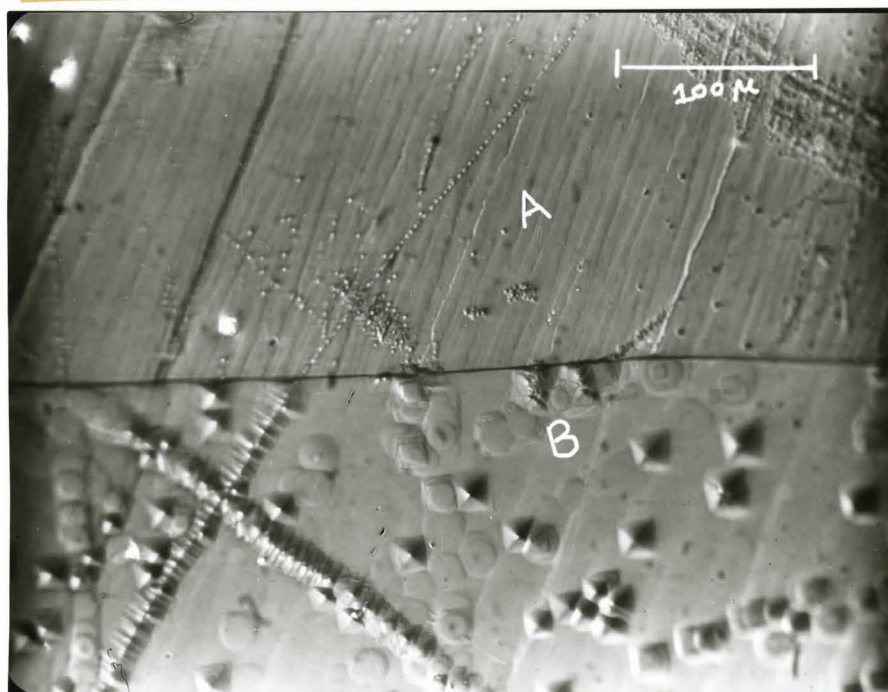


Fig. 24 Figure represents A and B bombarded at a dose of 10^{15} ions/cm² and etched for 5 sec and 25 sec in a 10 ppm Fe⁺⁺⁺ solution. Mag. 256X.

Fig. 25 A and B are unbombarded surfaces etched for 5 sec and 25 sec respectively (opposite face of the same sample as in fig. 24). Mag. 256X.

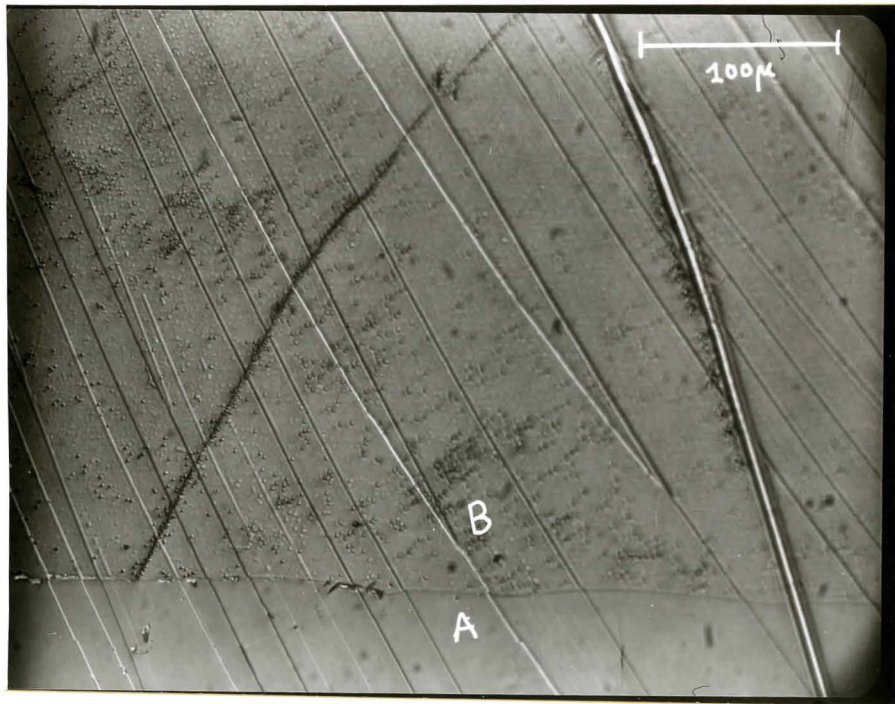


Fig. 26 A is unetched surface. B is bombarded by a dose of 10^{14} ions/cm² and etched for 3 seconds in a 10 ppm Fe⁺⁺⁺ solution. Mag. 256X.

Fig. 27

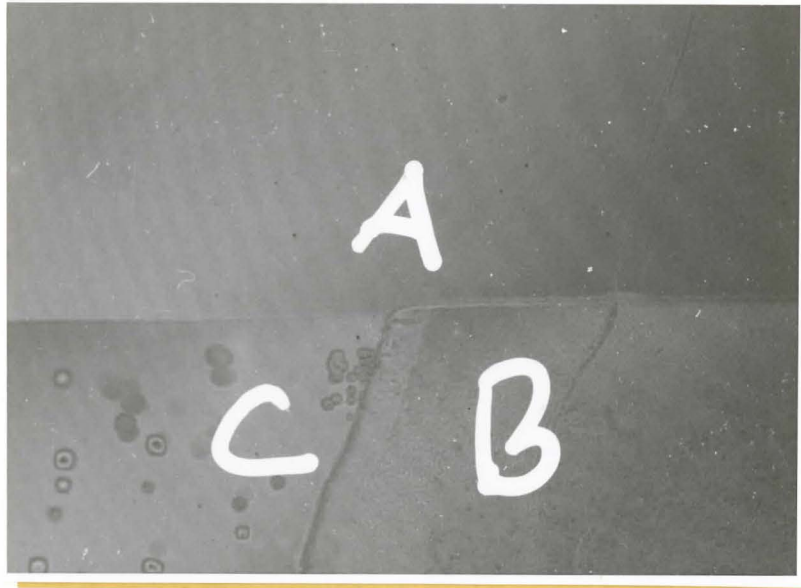


Fig. 28

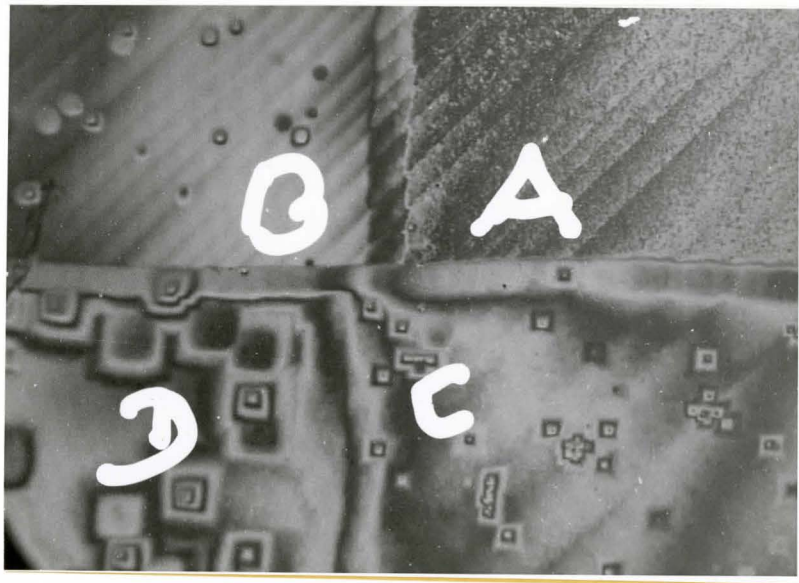


Fig. 27 Interference micrograph of the sample represented by fig. 22.

Fig. 28 Interference micrograph of the sample represented by fig. 23.

Fig. 29



Fig. 30

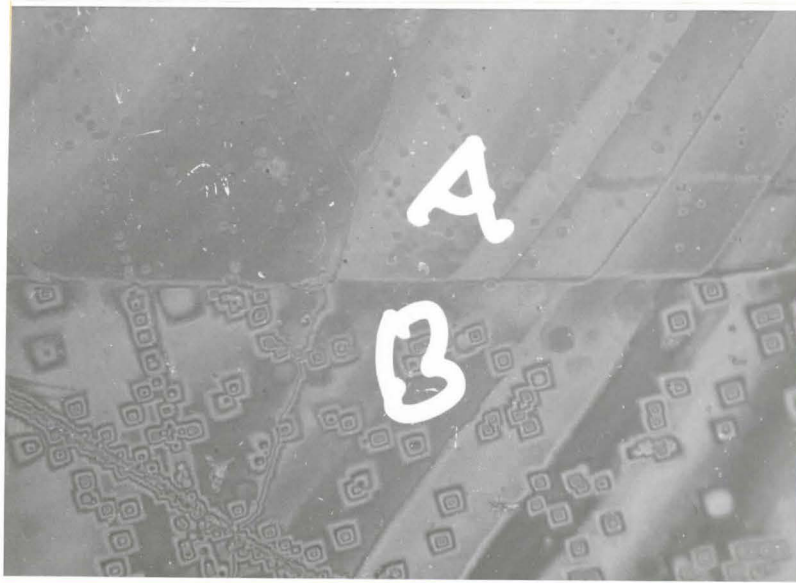


Fig. 29 Interference micrograph of the sample represented by figure 24.

Fig. 30 Interference micrograph of the sample represented by figure 25.

Fig. 31A

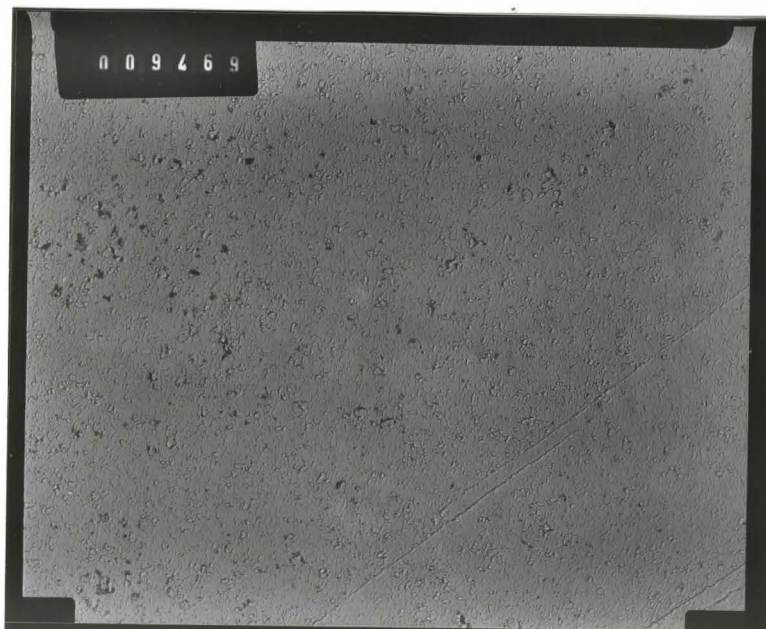


Fig. 31B

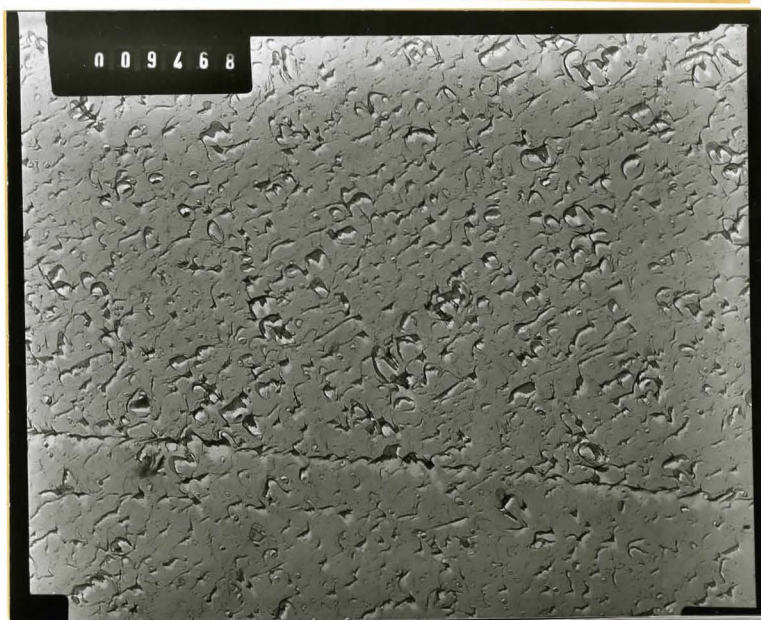


Fig. 31 Replica electron micrograph of the region B of fig. 22 and A of fig. 23.

A → Mag., 2,500X

B → Mag., 500X

Fig. 31C

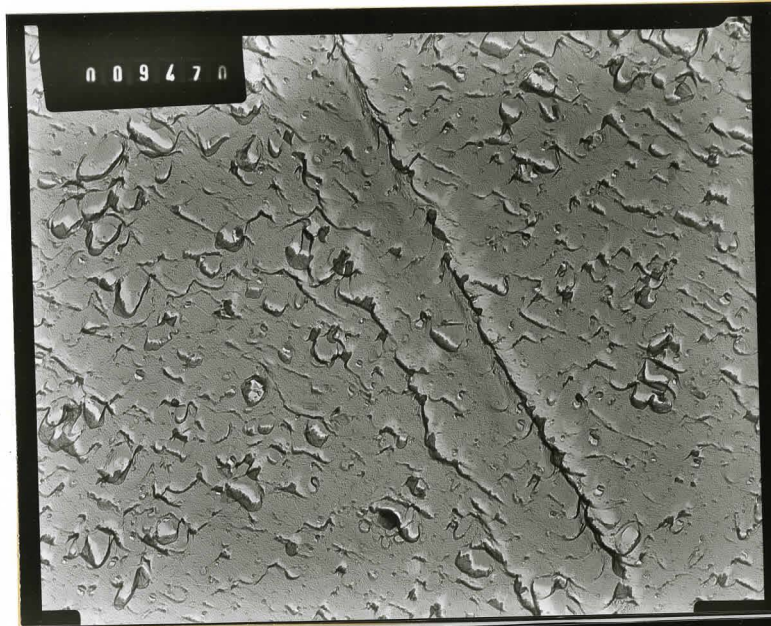
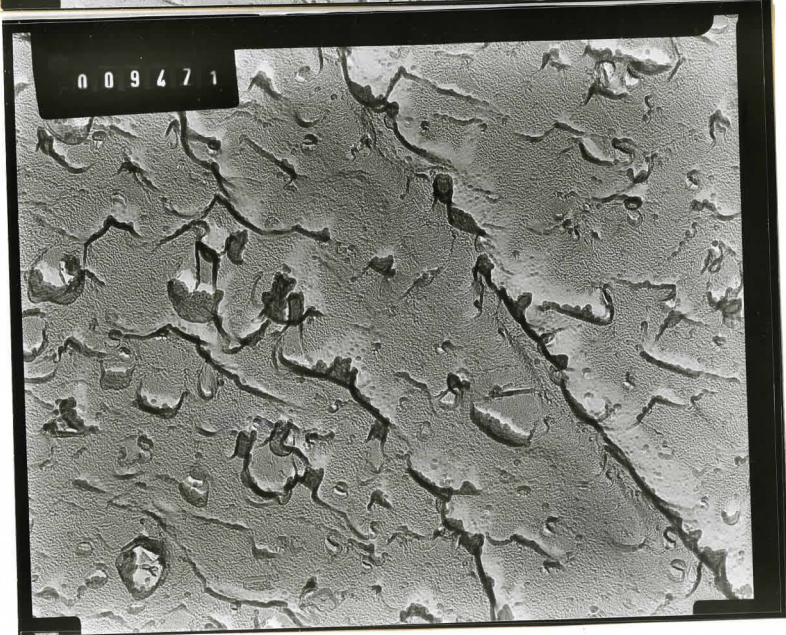


Fig. 31D



C → 10,000X

D → 22,500X

Fig. 32A

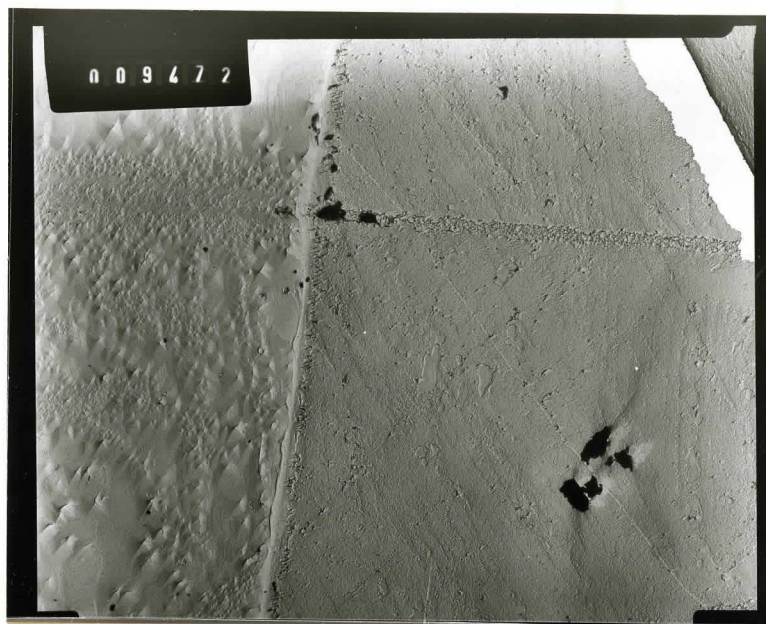


Fig. 32B

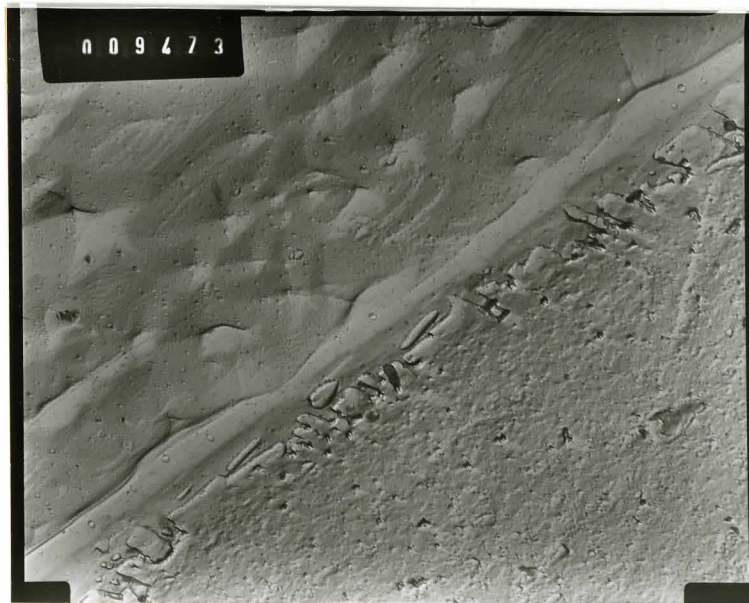


Fig. 32 Replica-electron micrograph of a sample bombarded at a dose of 10^{15} ions/cm² and etched in a 10 ppm Fe⁺⁺⁺ solution.

A → A junction of the bombarded surface after 5 sec and 25 sec etch. Mag. 2,500X.

B → Same junction at 7,500X.

Fig. 32C

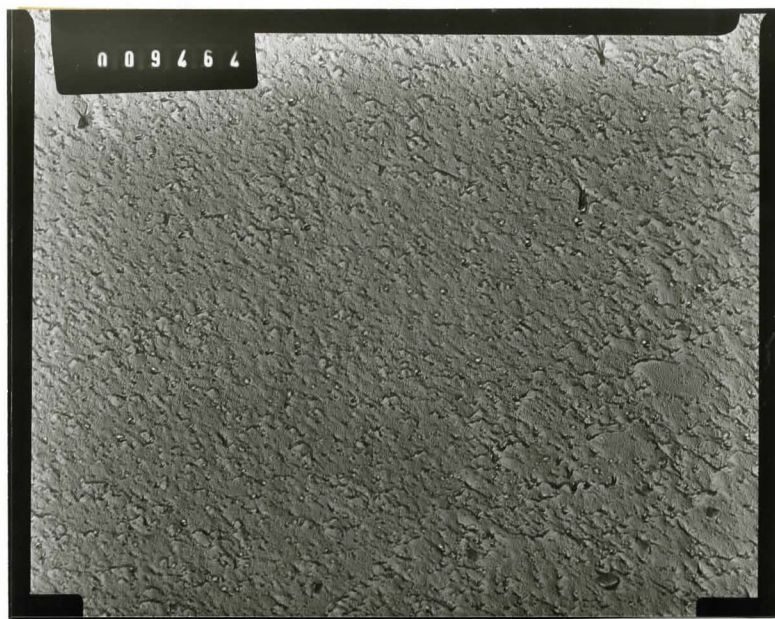
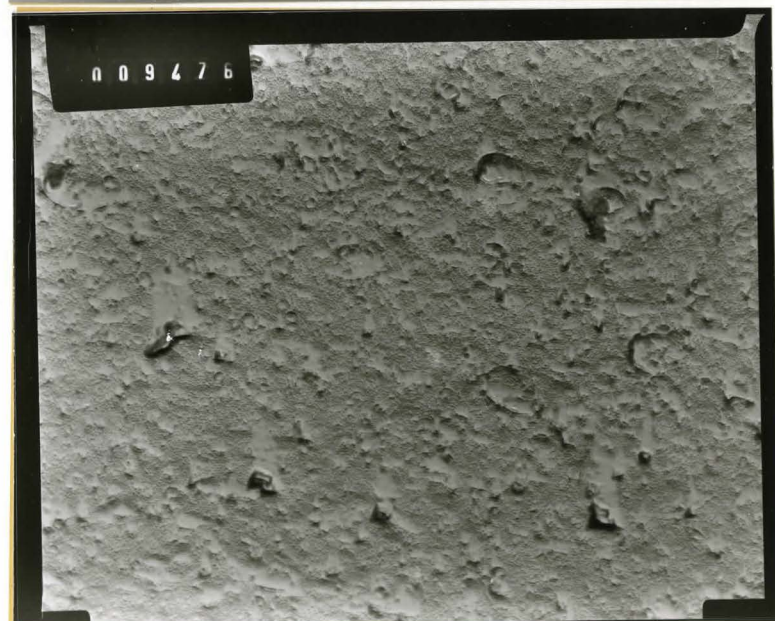


Fig. 32D



C and D → Bombarded surface after 5 sec etch. Mag.
10,000X and 22,500X respectively.

Fig. 33A

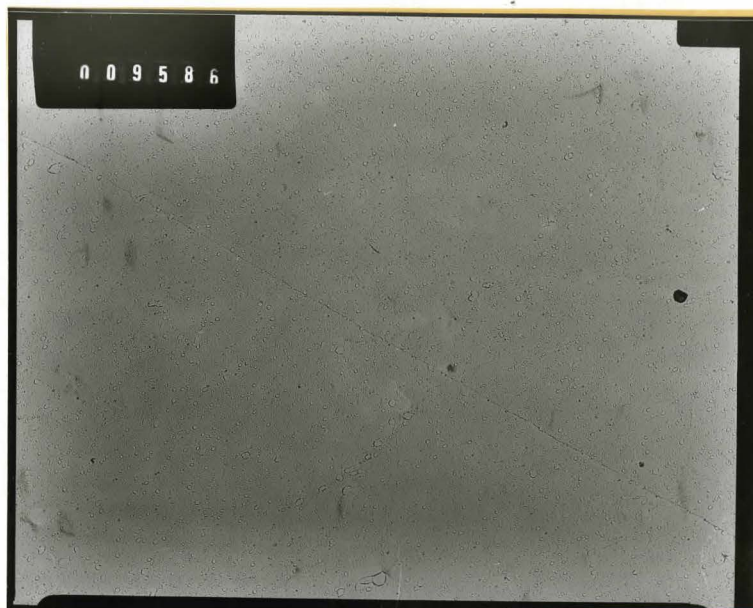


Fig. 33B

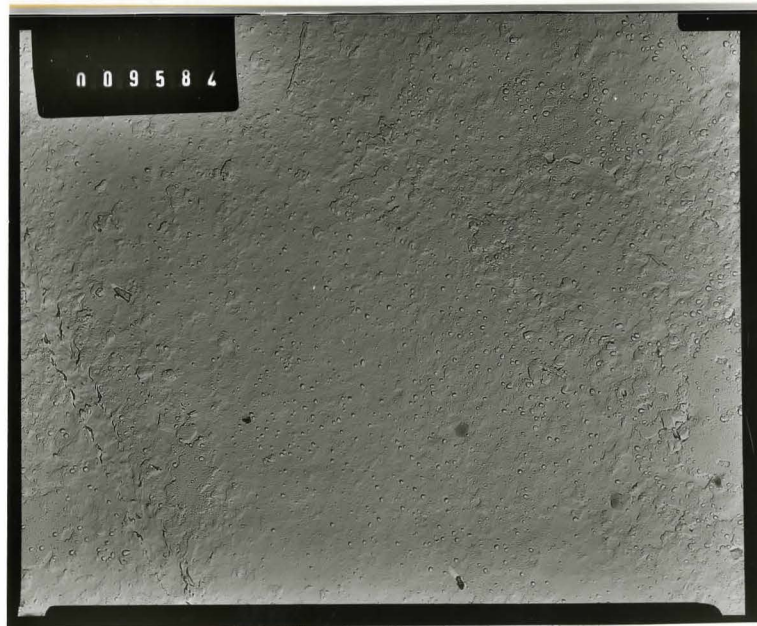


Fig. 33A An electron micrograph after zero second etch.
Mag. 5000X.

Fig. 33B An electron micrograph after 5 second etch.
Mag. 5000X.

Fig. 33C

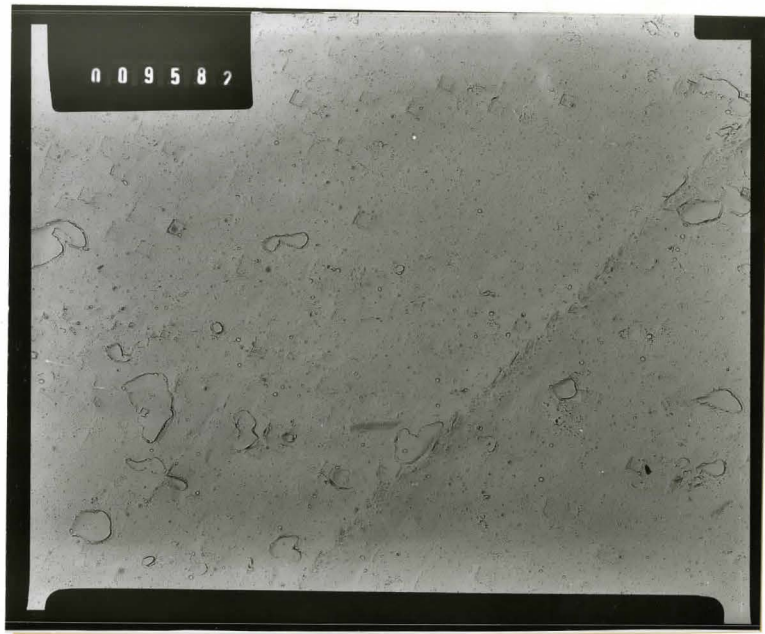


Fig. 33C An electron micrograph after 10 second etch.
Mag. 5000X.

Fig. 33D

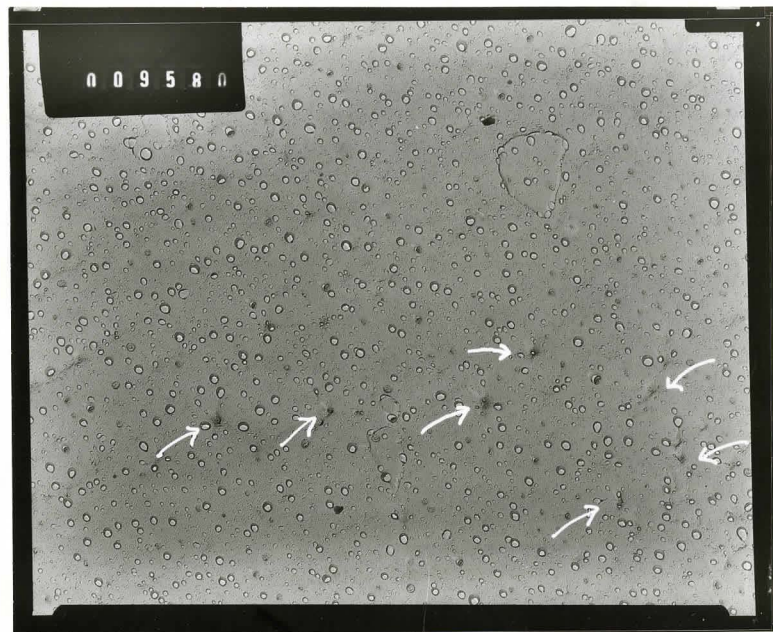


Fig. 33E

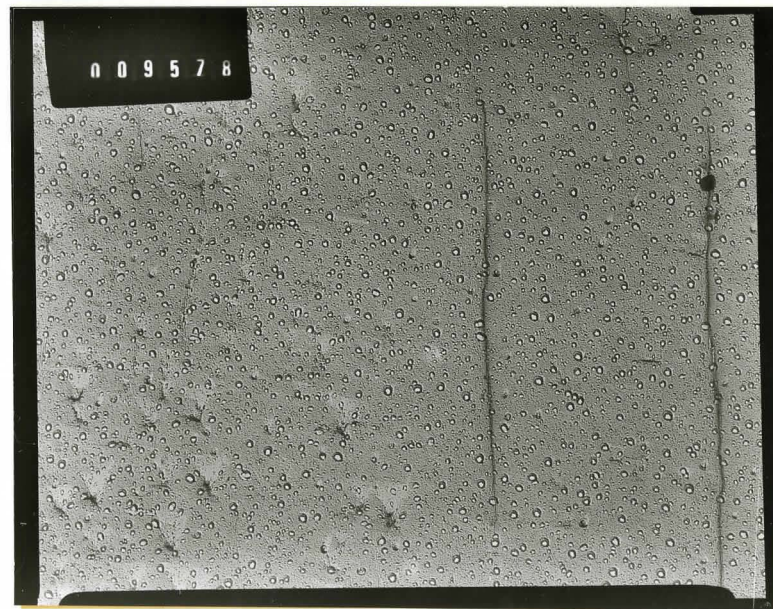


Fig. 33D An electron micrograph after 15 second etch.
Mag. 5000X.

Fig. 33E An electron micrograph after 20 second etch.
Mag. 5000X.

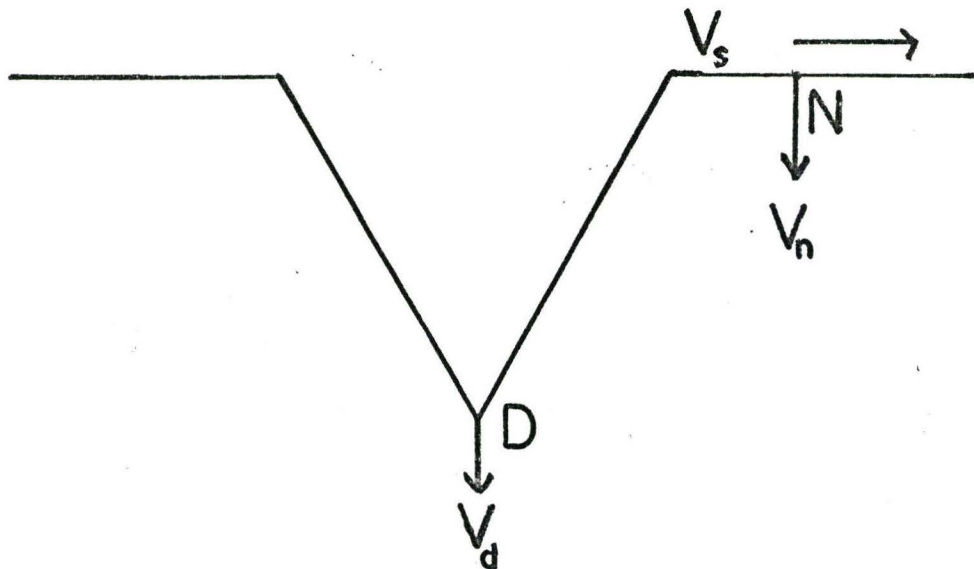


Fig. 34 A sketch showing a preferential attack at a dislocation site.

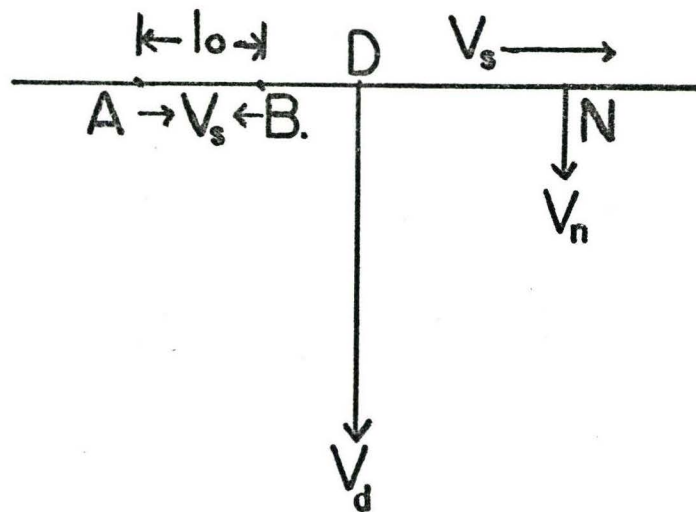


Fig. 35 A sketch to estimate critical distance between two dissolution nuclei for a non-preferential attack at a dislocation site.